2012-03-14

Numerical Investigation of Internal Wave-Vortex Dipole Interactions

Tyler D. Blackhurst
Brigham Young University - Provo

Numerical Investigation of Internal Wave-Vortex Dipole Interactions

Tyler D. Blackhurst

A thesis submitted to the faculty of
Brigham Young University
in partial fulfillment of the requirements for the degree of

Master of Science

Julie C. Vanderhoff, Chair
Steven E. Gorrell
Tadd T. Truscott

Department of Mechanical Engineering

Brigham Young University

April 2012

ABSTRACT

Numerical Investigation of Internal Wave-
Vortex Dipole Interactions

Tyler D. Blackhurst
Department of Mechanical Engineering, BYU
Master of Science

Three-dimensional linear ray theory is used to investigate internal waves interacting with a Lamb-Chaplygin pancake vortex dipole. These interactions involve waves propagating in the same (co-propagating) and opposite (counter-propagating) horizontal directions as the dipole translation. Co-propagating internal waves in the vertical symmetry plane between the vortices of the dipole can approach critical levels where the wave energy is absorbed by the dipole or where the waves are overturned and possibly break. As wave breaking cannot be simulated with this linear model, changes in wave steepness are calculated to aid in estimating the onset of breaking. Counter-propagating internal waves in the vertical symmetry plane can experience horizontal and vertical reflections, including turning points similar to waves in two-dimensional steady shear. Wave capture is also a possible effect of either type of interaction, depending on initial wave properties and positioning relative to the vortex dipole. Away from the vertical symmetry plane, a spanwise converging (focusing) and diverging (defocusing) of wave energy is observed in co- and counter-propagating interactions as symmetric off-center rays interact with the dipole's individual vortices. Some off-center rays experience multiple horizontal refractions similar to wave trapping.

Keywords: internal waves, Lamb-Chaplygin, vortex dipole, interaction, ray tracing, focusing, defocusing, critical level, turning point, wave capture, wave trapping

ACKNOWLEDGMENTS

As my advisor, Julie C. Vanderhoff has had infinite patience with me as she deepened my understanding of the physical world (and especially while I simultaneously studied the dark side). For this, I give her my deepest appreciation. After four years of working together, I consider her one of my great friends and hope that at some time I contributed something of value to her and her work.

I thank Steven E. Gorrell and Tadd T. Truscott for being on my graduate committee and for their advice and direction in the completion of this research and thesis.

To Erin, Luke, and Jake I give my most heartfelt love, eternal devotion, and absolute gratitude for their unending support. I could not have done this without them because I do it for them.

I thank my parents, Doug and Elaine, for instilling in me the work ethic and motivation to earn a strong and complete education, of which this is only the beginning. I also thank a host of family members, immediate and extended, who have supported Erin and me in many ways, but especially with their prayers and love.

I acknowledge the grant support of the Rocky Mountain NASA Space Grant Consortium (2008-2010) and the ASME Marjorie Roy Rothermel Scholarship (2008-2009).

TABLE OF CONTENTS

LIST OF TABLES

LIST OF FIGURES

CHAPTER 1. INTRODUCTION

Internal waves play an integral role in oceanic and atmospheric dynamics because of their size ranges (limited vertically only by the fluid boundaries and horizontally they are virtually without constraint [1]) They are also a source of turbulence and mixing [2] and affect climate and weather patterns [3]. They are crucial in maintaining environmental energy budgets (i.e., mass, momentum, and heat). For example, an estimated 2.1 terawatts of energy is required to balance the ocean's thermohaline circulation to avoid stagnation [4]. This comes from many sources, including solar radiation, wind across the ocean surface, temperature gradients, and the rotation of the earth. But it is difficult to know how this energy dissipates. It has long been known that at least some dissipation is due to friction over topography in places of shallow water [5]. It has since been shown that more than half of the dissipation occurs in the deep ocean, especially near rough topography [6]. This is most likely a result of internal wave generation, propagation, and breaking [7]. Understanding the effects of internal waves is essential in assessing climate changes and in creating accurate weather models, serving meteorology and aerospace, academia and industry.

1.1 Internal Waves Characteristics

Internal waves propagate only in continuously stably stratified fluids [7], fluids in which the density increases with depth, such as the earth's ocean and atmosphere. Ocean stratification below the surface mixed layer (approximately 200 meters [8]) is nearly linear (about 13.5% change in density per kilometer) and is primarily a result of differences in temperature and salinity [9]. Except for the planetary boundary layer, where weather mostly occurs and mixing is dominant, most of the atmosphere is stably stratified [10], especially in the strongly-stratified stratosphere [11], though the stratification is not linear (on average, about 10.5% change in density per kilometer [9]).

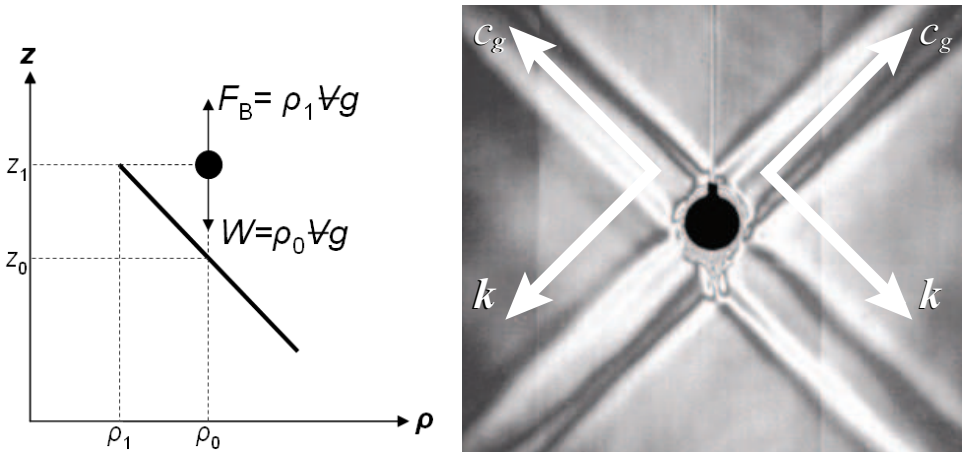

(a) (b)

Figure 1.1: (1.1(a)) Two-dimensional schematic showing the mechanics involved when a particle, having density ρ_0, of a stratified fluid is vertically displaced from its neutrally-buoyant depth at z_0. The solid line represents a linear density distribution for the fluid. As energy propagates through the fluid, oscillations of fluid particles all along isopycnals describe the propagation of internal waves. (1.1(b)) A vertically-oscillating horizontal cylinder is oriented in and out of the page and is seen in the middle of the image (black spot). Perturbing a stratified fluid, the cylinder generates four beams of internal waves each propagating away from the cylinder in the direction labeled $\boldsymbol{c}_g$. The phases of the internal waves are seen as black and white lines running parallel to and within the beams and propagating in a direction perpendicular to $\boldsymbol{c}_g$, labeled $\boldsymbol{k}$. For the lower beams, $\boldsymbol{k}$ is upward and perpendicular to the beams.

A fluid may be described as having layers of constant density, or isopycnals, stacked one on top of another, lighter-density fluid on heavier. Stratification prevents vertical mixing of isopycnals when the fluid is disturbed. Instead, fluid particles displaced vertically from their neutrally-buoyant layer will oscillate resultant of the restoring forces of gravity and of buoyancy. The mechanics of this motion are depicted in Figure 1.1(a), which shows a particle of a stratified fluid having a linear density distribution given by the solid line. Due to some perturbation in the fluid, the particle, having density ρ_0, has been displaced from its neutrally-buoyant layer at z_0 to z_1, where the density is ρ_1. The weight of the particle $W = \rho_0 \forall g$, where $\forall$ is the volume of the particle and g is the constant of gravitational acceleration, pulls down on the partcle while the buoyant force $F_B = \rho_1 \forall g$, where ρ_1 is the density of the surrounding fluid, pulls up. Because $\rho_1 < \rho_0$ when the particle has been displaced upward from its origin, $W > F_B$. Thus, after the particle's upward motion resultant of the perturbation has ceased, its weight will pull it down toward z_0. If the perturbation is strong enough or if the particle's weight is large enough, the now downward momentum of the particle

may be large enough that the particle will descend past it's neutrally-buoyant fluid layer at z_0 and into layers of denser fluid. Here, $F_B > W$ and the fluid particle will eventually change direction again. These oscillations continue as long as there is energy to sustain them.

As the energy propagates through the fluid, particles along isopycnals will experience these oscillations. The rhythmic motion of the phase propagation along the isopycnals, at least in two dimensions, is similar to that of a plane wave propagating along a string or wire and describes the propagation of internal waves. In three dimensions, the motion is more circular. The generation of internal waves can be visualized in the image of Figure 1.1(b). A vertically-oscillating horizontal cylinder, oriented in and out of the page and seen in the middle of the image (black spot), perturbs a stratified fluid. The internal waves are seen as four beams of energy propagate away from the cylinder; the directions of internal wave energy propagation for two of the beams are labeled $\boldsymbol{c}_g$ (discussed below). The other two beams have not been labeled so to not obscure the view of all the beams. The phases of an internal wave beam, especially the crests and troughs, are seen as white and black lines parallel to and within the beam. These propagate perpendicular to $\boldsymbol{c}_g$ in the directions labeled $\boldsymbol{k}$ (discussed below). In the cases of the lower beams, the direction of $\boldsymbol{k}$ is upward and perpendicular to the beams.

The stability and strength of the stratification within a fluid can be considered by applying Newton's second law of motion to a fluid particle vertically displaced a distance $\eta(t)\cos\theta$, where t represents time and θ is the angle from the vertical, within an incompressible fluid having a density distribution $\bar{\rho}(z)$ yields the second-order differential equation

$$\frac{\partial^2 \eta(t)}{\partial t^2} - \frac{g}{\rho_0}\frac{\partial \bar{\rho}(z)}{\partial z}\eta(t)\cos^2\theta = 0 \tag{1.1}$$

where g is the constant of gravitational acceleration, ρ_0 is a reference density within the hydrostatically-balanced fluid (typically the density of the displaced particle), and z is the upward-positive coordinate. The coefficient in the second term defines the stability and strength of the stratification. It is known as the Brunt-Väisälä frequency, commonly called the natural, or buoyancy, frequency,

$$N^2 = -\frac{g}{\rho_0}\frac{\partial \bar{\rho}(z)}{\partial z} \tag{1.2}$$

Where $\partial\bar{\rho}(z)/\partial z$ is negative, N is positive and there exists a stable stratification [9]. If $|\partial\bar{\rho}(z)/\partial z|$ is large, N is also large and the stratification is strong, inhibiting vertical mixing of the fluid. If perturbations in a continuously, stably stratified fluid are sufficiently slow to oscillate fluid particles at a frequency less than the buoyancy frequency, but greater than the global rotational frequency of the medium (e.g., the Coriolis frequency in geophysical flows), energy of the flow is transferred to the generation and subsequent propagation of internal waves.

The frequency at which the perturbed fluid particles oscillate describes the phase propagation of the generated internal waves. It is known as the relative frequency ω_r because it is measured relative to the frame of reference moving with the medium, or background flow, in which the internal waves propagate or with which they interact. The background may be a steady wind or current, much larger-scaled internal waves, or another phenomenon in the fluid, as previously mentioned. The relative frequency is determined from the dispersion relation

$$\omega_r^2 = \frac{N^2\left(k^2+l^2\right)+f^2m^2}{k^2+l^2+m^2} \tag{1.3}$$

where f is the global rotational frequency of the medium and $\boldsymbol{k} = (k,l,m)$ is the wavenumber vector, which defines the direction of phase propagation. The total frequency Ω of the internal waves is the wave frequency observed from a stationary frame of reference. It is related to the relative frequency through the Doppler relation

$$\Omega = \boldsymbol{k}\cdot\boldsymbol{V} + \omega_r \tag{1.4}$$

where $\boldsymbol{V} = (U,V,W)$ is the velocity of the background flow.

Figure 1.2 gives an idealized representation of propagating internal waves. Various wave properties are labeled for reference. Though the schematic is limited to two dimensions, it conveys ideas that can and should be considered in three dimensions for internal waves. Internal waves propagate in groups, or packets, the size of which is defined by the length of time conditions allowed for the generation of internal waves as discussed above. The dotted curves in the schematic represent the boundaries of the wave packet, commonly referred to as the packet envelope. The increasing-decreasing pattern of the wave amplitude a is resultant of the packet confining the waves

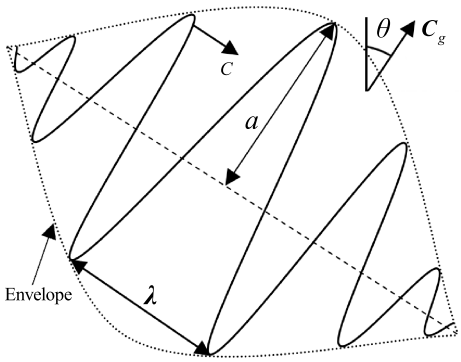

Figure 1.2: Schematic of two-dimensional packet of internal waves. Properties are labeled for reference.

as the crests and troughs of the waves propagate at the phase speed c within the packet. A phase speed is defined in each spatial dimension, but they do not collectively form a velocity vector.

Inversely proportional to the components of the wavenumber vector $\boldsymbol{k}$ are the components of the wavelength vector $\boldsymbol{\lambda} = 2\pi/\boldsymbol{k}$, which defines the length between two points in phase with each other, such as two adjacent crests or troughs. The components of these vectors are measured relative to the typical spatial axes, and not to the wave packet itself. Wavelengths of internal waves vary in scale from meters to hundreds of kilometers. Due to natural boundaries in the vertical (e.g., fluid surfaces or interfaces), the horizontal wavelengths can be much larger than the vertical wavelengths.

The wave packet carries the wave energy in a direction perpendicular to the direction of phase propagation and at the angle

$$\theta = \cos^{-1} \frac{\omega_r}{N} \tag{1.5}$$

which is measured from the vertical and is related to all of the wave properties through the dispersion relation. When waves refract, the propagation angle changes with the wavenumbers, altering the relative frequency. The velocity of the wave packet, and thus of the wave energy propagation, is the group velocity

$$\boldsymbol{c}_g = \nabla_{\boldsymbol{k}} \omega_r = \left(\frac{\partial \omega_r}{\partial k}, \frac{\partial \omega_r}{\partial l}, \frac{\partial \omega_r}{\partial m} \right) \tag{1.6}$$

As internal waves interact with other fluid phenomena, their chacteristics and properties may be affected. Because the focus of this thesis is a particular type of internal wave interaction, it is important to understand these basics of internal wave generation and propagation.

1.2 Motivation

The generation of internal waves results from a wide variety of sources, including flow over topography [12], the collapse of mixed fluids [13], and turbulence [14]; they have even been found generated within vortices [15] and as the result of colliding vortex dipoles [16]. The ensuing internal wave propagation is as distinct as the wave properties, and the evolution of wave properties will depend on the conditions of the flow in which the internal waves propagate, i.e., the background flow [17] (see Nappo [10] for an excellent general description). With so many phenomena existing in the ocean and atmosphere, internal wave interactions are inevitable. It is of interest, then, to study a variety of internal wave interactions and understand the effects of the background flow on internal waves and vice versa. Results of such studies can then be applied to understanding the effects on climate and weather.

The large, horizontal motions of internal waves cause overturning and instabilities as flows shear and layers of lighter fluid are pulled under layers of heavier fluid. Specifics of these instabilities depend on the wave amplitude and direction of propagation [18]. Waves may then break, generating turbulence [19]. As information regarding mechanisms ushering wave breaking in the ocean and atmosphere is collected, an understanding of the subsequent energy dissipation may come without the painstaking computations required in modeling small-scale energy dissipations, but rather from modeling the large-scale motions of internal waves [20]. Understanding these motions under an array of circumstances and interactions provides the details necessary to develop such models.

A commonly studied interaction involves internal waves propagating through a current. Geostrophic currents have vertical and horizontal shears that may cause internal waves to approach turning points and critical levels [21]. Critical levels are depths in the fluid where the vertical group speed asymptotically approaches zero because the relative frequency ω_r of the internal waves approaches the minimum value possible, which is the global rotational frequency of the medium (e.g., the Coriolis frequency in geophysical flows). Turning points are depths in the fluid where vertical reflections occur because the relative frequency ω_r of the internal waves approaches the maximum value possible, the buoyancy frequency N of the fluid. Either interaction may solicit instabilities [22, 23]; or, in the case of a critical level, the background may gradually absorb the wave

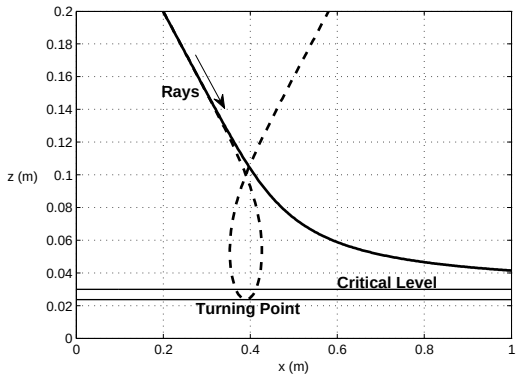

Figure 1.3: Ray tracing tracks the positions through time of two rays initially propagating at $x = 0.2$ m from right to left and downward as indicated by the arrow. The solid ray bends to the horizontal as it approaches a critical level at about $z = 0.03$ m as ω_r approaches zero. The dashed ray bends to the vertical until reflecting at a turning point at about $z = 0.024$ m as ω_r approaches N.

energy [24]. Such consequences are not limited to this type of interaction and will be discussed in reference to the research involved in the current study.

Ray tracing is a relatively simple way of tracking through time the position and property changes of an internal wave packet as it interacts with a specified background. Figure 1.3 shows two rays traced in space while interacting with a steady shear flow, or current. Each initially propagates at $x = 0.2$ m from right to left and downward as indicated by the arrow. The solid ray propagates horizontally in the same direction as the shear and bends to the horizontal as the interaction progresses, asymptotically approaching a critical level at about $z = 0.03$ m. The dashed ray propagates horizontally in the opposite direction as the shear and bends to the vertical until reflecting a turning point at about $z = 0.024$ m. The loop occurs as the shear continues to interact with the wave packet as it propagates upward and to the right. The wave packet ceases interacting with the shear where the angle of the ray no longer changes.

Godoy-Diana, Chomaz, and Donnadieu [25] conducted two experimental cases of internal wave beams interacting with a horizontal Lamb-Chaplygin pancake vortex dipole given an approximately Gaussian vertical distribution of velocity. In one case, beams of internal waves propagating in the same horizontal direction as the translation of the vortex dipole (co-propagating) were observed bending to the horizontal and the wave energy was presumably absorbed by the dipole at a critical level at depth z_C. In the other case, internal waves propagating horizontally

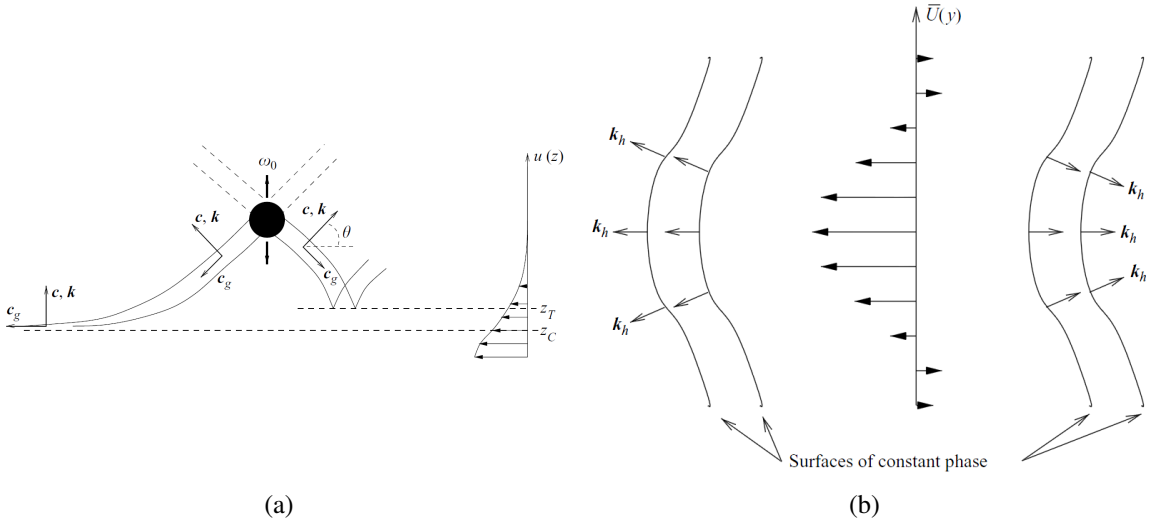

Figure 1.4: (1.4(a)) Sketch of a cylinder generating internal wave beams (Figure 1 of Godoy-Diana, et al. [25]). The top half of the Gaussian velocity profile enveloping the dipole is shown. Also sketched are the wave-vortex interactions along the vertical symmetry plane: the co-propagating beam of internal waves is absorbed at a critical level at depth z_C and the counter-propagating beam of internal waves is reflected at a turning point at depth z_T. (1.4(b)) Schematic showing defocusing of co-propagating wave energy (left) and focusing of counter-propagating wave energy (right) in the horizontal midplane (Figure 16 of Godoy-Diana, et al. [25]). The mean velocity profile is shown (middle) spanning the plane.

opposite to the direction of dipole translation (counter-propagating) reflected vertically at a turning point at depth z_T. These phenomena both occurred in the vertical symmetry plane separating the dipole's counter-rotating vortices (see Figure 1.4(a)). Outside of this plane, the horizontal structure of the dipole caused spanwise divergence, or defocusing, of the internal wave beam in co-propagating interactions and spanwise convergence, or focusing, in counter-propagating interactions (see Figure 1.4(b)). Though the experiment was fully three-dimensional, the observations were two-dimensional because the viewing techniques were limited to the vertical symmetry plane and the horizontal midplane of the dipole.

1.3 Objectives

This thesis details the work and results of three-dimensional ray theory simulating co- and counter-propagating interactions of internal waves with a Lamb-Chaplygin pancake vortex dipole of constant rotation and translation in a linearly-stratified fluid. Dynamics of internal wave-vortex

dipole interactions are explored throughout the three-dimensional domain. Though ray theory is linear, the trajectories are accurate [26] and increase comprehension of internal wave-vortex interactions. Ray theory does not measure the amplitudes of the waves, but a secondary method is used, calculating wave steepness as the change in wave amplitude over the change in depth. This allows for the estimations of the onsetting of nonlinear effects, such as overturning [19].

Comparisons of the ray theory results are made with the results of the experiment. Through ray theory, this study confirms the possibility of critical levels in the vertical symmetry plane of the co-propagating dipole. It also shows wave capture [27] is possible and may be mistaken for a critical level because of their spatial similarities. For counter-propagating interactions, turning points are possible in the vertical symmetry plane, but wave capture is again possible if the turning point does not complete. The advantage of three-dimensional ray tracing is complete in considering rays propagating outside the vertical symmetry plane. It is found that focusing and defocusing are not limited to counter- and co-propagating interactions, respectively, but that they are a function of the initial wave properties and the initial position of a wave packet relative to the dipole. What's more, this ray tracing indicates wave trapping [28] for many off-center rays.

CHAPTER 2. LITERATURE REVIEW

2.1 Two-Dimensional Internal Wave Studies

Internal wave interactions are abundant in the ocean and atmosphere, and are commonly studied experimentally and computationally. Such studies are traditionally two-dimensional due to physical and computational limitations. Nevertheless, much has been learned about internal wave propagation and the numerous possible interactions. This section provides a few examples of studies on internal waves in two dimensions.

Internal waves may interact with other internal waves of similar and differing scales. Using ray theory, Broutman [29] considered the refraction of internal waves as they pass through inertial waves (large-scale, low-frequency internal waves), which, due to their immense size, produce a horizontal current locally experienced by the internal waves. As the internal waves pass through the inertial waves, they also experience the upward motion due to the phase propagation of the inertial waves. The group speed of the internal waves may then approach the phase speed of the inertial waves. This depth, called a caustic, is horizontal relative to the inertial waves and is impassable by internal waves. Instead, internal waves can experience vertical reflection and permanent alterations to their wave properties. Depending on initial values of internal wave properties, energy of the internal waves may be absorbed by the inertial waves. Wave overturning and breaking are also possible as the wave steepness increases during the approach to the caustic.

In some cases, simply disturbing the internal waves propagating in a quiescent fluid may change wave properties sufficiently to cause instabilities. Thorpe [30] defined a Richardson number as the ratio of the strength of the fluid's stratification to the wave steepness of the internal waves. A critical Richardson number was found to estimate instabilities of the internal waves. For disturbances in the transverse direction of internal wave propagation, the critical Richardson number decreases with increasing steepness and must be sufficiently smaller than $1/4$ before instabilities will develop. For disturbances in the same direction of internal wave propagation, the

critical Richardson number is $1/4$ for all wave steepness values less than unity. Resultantly, it is these disturbances which first grow as steepness increases. Also, these disturbances increase the wave steepness even before the onset of the instability. However, when wave frequency is much less than the Coriolis frequency the disturbances of both directions become unstable for nearly the same steepness value. This confirms previous studies showing that wave breaking is by shear instability and the disturbance growth rates are practically independent of their direction.

Internal waves may also interact with topographical features, including reflecting off of a sloped boundary. Slinn and Riley [31] found internal waves transition to turbulence when reflecting from a sloped boundary having an angle matching the angle of internal wave propagation. They show this mixing process has an efficiency of about 35% and suggest the turbulence resulting from such an interaction makes a signifiant contribution to ocean mixing. Steeper topography may yield stronger turbulence and transtitions for Reynolds number of $1,000$, whereas terrain that is more shallow requires much higher Reynolds numbers.

Studies of internal waves in accelerating flows further yield information on internal wave instabilities, including expected locations and circumstances. Thorpe [32] showed that the Richardson number relative to an instability in a flow of small acceleration may surpass the critical Richardson number, increasing the likelihood of instabilities and wave breaking. In a later, but related study, Bouruet-Aubertot and Thorpe [33] showed that accelerating flows cause internal waves to approach the area of the flow with greatest acceleration. There, a growth of small-scale density fluctuation may cause wave overturning. The cause is the energy transfer between the internal waves and the accelerating flow. The results of this interaction are similar to that of internal waves in a steady shear, but they happen more quickly.

A variety of phenomena may occur when internal waves interact with vortices. In particular, Bühler and McIntyre [34] have introduced the concept of wave capture (see Figure 2.1), for which an internal wave packet is caught into the flow between counter rotating vortices and the horizontal component of the group velocity approaches the translational speed of the dipole as the horizontal and vertical wavenumbers k and m approach infinity. The internal wave packet becomes inseparable with the background. Wave-vortex duality occurs; that is, the internal wave packet resembles a vortex-dipole by creating a return-flow dipole in the mean flow. This nonlinear interaction causes the internal waves to yield their wave energy to the dipole. At this point, should the

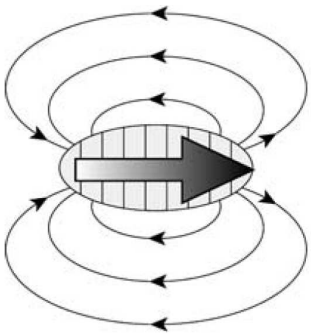

Figure 2.1: Schematic giving the top-down view of an internal wave packet (represented by the ovular object circumscribing the large arrow) approaching wave capture as it propagates horizontally in the same direction as the vortex dipole translation (left to right) and along the plane uniting the vortices of the dipole (Figure 3*a* of Bühler and McIntyre [34]). The motion of the vortices is represented by the ovular curves with arrows.

wavepacket ever dissipate, it does not give its momentum to the background. Rather, any energy exchange and dissipation has already occurred during the prior steps of the interaction.

As will be seen later, wave capture may physically resemble the approach of an internal wave packet to a critical level, but the changes to the wave properties are different. During wave capture, the relative frequency does not decrease, but rather increases. Ray theory predicts that it eventually plateaus below the buoyancy frequency because both the horizontal and vertical wavenumbers are unbounded. Their model also suggests that, as long as a critical level doesn't first occur, the wave amplitude will approach infinity resultant of wave capture. Even then, wave breaking is not expected [34].

2.2 Three-Dimensional Internal Wave Studies

Numerical models facilitate the comparison of results with what is collected through observation and experimentation. However, reconciling theoretical predictions with experimental data can be problematic since theory and experimentation are sometimes simplified for two-dimensional scenarios while internal waves inherently propagate in three dimensions. It follows that three-dimensional simulations, although they require more computational time, yield more complete studies of the generation, propagation, and evolution of internal waves and can greatly increase knowledge of the related mechanics. Moreover, computing power has increased such that it is rarely a limitation to studying internal waves and their interactions.

Marks and Eckermann [35] applied three-dimensional ray tracing to a global atmosphere model by considering a rotating, stratified, and compressible three-dimensional atmosphere. Not only was the WKBJ approximation augmented to consider all wave frequencies (improving the model for dispersion and refractions), but a physcially realistic equation for wave steepness was applied to consider effects of radiative and turbulent wave damping. The model was compared to exploratory experiments which considered the effect of adding new model features. Because the dispersion relation was more complete, they found a reduced high-frequency cutoff due to decreasing horizontal wavenumber. They also showed greater significance in turbulent damping than radiative damping for a range of vertical and horizontal wavelengths and frequencies in most of the middle atmosphere.

Winters and D'Asaro [36] used a high-resolution, two-dimensional model to numerically simulate the evolution of finite-amplitude internal waves interacting with a spatially slowly-varying mean shear flow. Small-amplitude waves near a critical level obeyed linear theory. They were almost completely absorbed by the background flow, resulting in the acceleration of the background near the critical level. This acceleration was strong enough, relative to the wave motion, to maintain wave stability and linearity throughout the interaction even though the vertical wavelength decreased. At higher amplitudes, waves overturned and became unstable. Prior to breaking, some instabilities surprisingly persisted for many buoyancy periods. The authors believed the reason for the perceived delayed breaking to be the two-dimensional assumption used in the simulation. This they later confirmed using a large-eddy simulation to examine in detail the same interaction in three dimensions [37]. They also found convective instabilities had yielded counter-rotating vortices, the effects of which were magnified by wave shear. Depending on wave amplitude, one-third of wave energy was found to reflect, one-third contributed to mean flow acceleration, and one-third dissipated as turbulence.

Two-dimensional studies can be especially limiting for many internal wave interactions. For example, a horizontal plane of a vortex may be used in simulating interactions of internal waves with the two-dimensional rotation, but this neglects the effect on internal waves that the multiple layers of the vortex, not to mention the fluid stratification, will undoubtedly have above and below that plane. Recognizing this, Moulin and Flór [28] gave three-dimensional ray-tracing results of interactions between large-scale internal waves and a Rankine-type vortex having a Gaussian

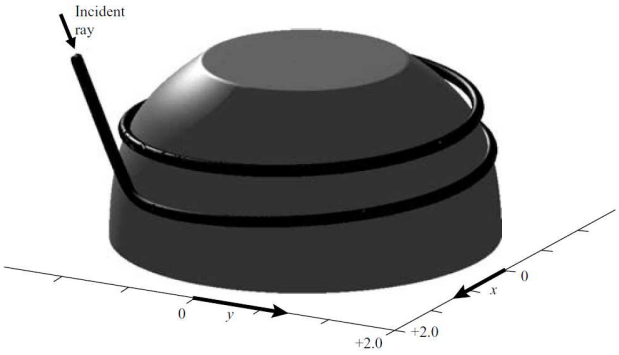

Figure 2.2: Three-dimensional schematic demonstrating wave trapping(Figure 3 of Moulin and Flór [28]). Depending on the relative strength of a vortex, an internal wave packet may be caught in the rotational motion of the vortex, as demonstrated by the ray circling the vortex (depicted by the solid object in the figure).

vertical distribution of vertical vorticity. Relatively weak vortices, defined by $k\text{Fr} < 1$, where k is the horizontal wavenumber and Fr is the Froude number, caused wave refraction while relatively strong vortices, $k\text{Fr} > 1$, trapped some waves in the rotational motion of the vortex (see Figure 2.2). Reflection was seen for $k\text{Fr} \approx 1$. If wave breaking does not occur first, internal waves may escape wave trapping.

In this thesis, three-dimensional ray tracing increases knowledge of the interactions of internal waves with a vortex dipole. It confirms much of what was experimentally observed [25], but it also provides new information only available by viewing the entire domain and not just a few planes. Chapter 3 illustrates the methods used to research wave-vortex interactions, including a presentation of the basics of ray theory and a two-dimensional application to introduce the application of ray tracing in Section 3.1, a review of the setup of the experimental counterpart of this study [25] in Section 3.2, and essential details of the Lamb-Chaplygin pancake vortex dipole in Section 3.3. Chapter 4 presents the results of three-dimensionally ray tracing co- and counter-propagating internal wave-vortex dipole interactions, which are compared and contrasted with the two-dimensional interactions with the steady shear given in Section 3.1 and with the experimental results. Chapter 5 closes the thesis with a discussion of main conclusions. An explanation of the validity of ray theory and the derivation of the linear Boussinesq Navier-Stokes equations are found in Appendices A and B, respectively.

CHAPTER 3. METHODS

3.1 Ray Tracing and Theory

Ray theory is a linear theory that traces in time and space the propagation of internal wave energy by assuming a packet of internal waves to be a point convected along a path, or ray [38]. It follows the evolution of the waves by tracking the changes of their properties during an interaction with a background flow and estimating the resultant motion. Ray theory applies the Wentzel-Kramer-Brillouin-Jeffreys (WKBJ) and the Boussinesq approximations. The former assumption allows the dispersion relation (Equation 1.3) to be locally valid. The latter neglects density changes except in terms where the acceleration due to gravity is a multiplier because differences in inertia of fluid particles are negligible except when gravity increases the effect of perturbations in the fluid. These assumptions simplify and solve the Navier-Stokes equations. The solution to the linear, Boussinesq Navier-Stokes equations (derived in Appendix B) is a form of the wave equation,

$$w = w_0 \cos(\boldsymbol{k} \cdot \boldsymbol{x} - \omega_r t) \tag{3.1}$$

where w is the verical component of the background velocity and the subscript 0 represents the inital value, $\boldsymbol{k}$ is the wavenumber vector, $\boldsymbol{x}$ is the spatial vector, ω_r is the relative frequency of the small-scale internal waves, and t is time.

Though not representative of all wave-vortex interactions, this solution is realistic when slowly-varying internal waves interact with much larger-scale background flows that are assumed unaffected by the interaction. The slowly varying approximation assumes small variation in changes of amplitude of internal waves in a packet. The scale separation hypothesis assumes the scales of the background flow to be sufficiently larger than those of the interacting internal waves so that the features of each phenomenon remain distinct and the background is unaffected. The method used to check validity of the slowly varying approximation within the WKBJ approximation is

incomplete for multiple dimensions and does not validate every ray in the internal wave-vortex dipole interactions of this study (see Appendix A for more details). Nevertheless, even those interactions which do not obey this assumption generally follow the spatial trajectory patterns observed experimentally by Godoy-Diana, et al. [25]. The scale separation hypothesis is assumed valid for this study because Godoy-Diana, et al. [25] only found insignificant changes to the vortex dipole which could be neglected. In any case, it has been shown that trajectories predicted by ray theory are accurate even when the scales of internal waves and the background are not sufficiently different [26].

The following is a review of ray theory. For a more extensive description, see Lighthill [39]. The dispersion relation (Equation 1.3, repeated for convenience)

$$\omega_r^2 = \frac{N^2\left(k^2+l^2\right)+f^2m^2}{k^2+l^2+m^2} \tag{3.2}$$

defines the relative frequency ω_r, the frequency of the internal waves in a frame of reference moving with the wave packet, where k, l, and m are the components of the wavenumber vector $\boldsymbol{k}$; $N \geq \omega_r$ is the buoyancy frequency of the fluid; and $f \leq \omega_r$ is the system's frequency of rotation (e.g., the Coriolis frequency in geophysical flows). In the case of a non-rotating system, as in this study, $f = 0\ \mathrm{s}^{-1}$.

As it is often inconvenient to track the interaction of internal waves in the frame of reference of the internal waves, the Doppler relation shifts the frame of reference to a stationary one as follows (Equation 1.4, repeated for convenience):

$$\Omega = \boldsymbol{k}\cdot\boldsymbol{V} + \omega_r \tag{3.3}$$

where Ω is the total frequency of the internal waves, constant along a ray [39], and $\boldsymbol{V} = (U,V,W)$ is the background velocity.

Equation 3.3 determines the total velocity of an internal wave packet, or group velocity, propagating in a moving fluid (compare to Equation 1.6) through the equation

$$\frac{d\boldsymbol{x}}{dt} = \nabla_{\boldsymbol{k}}\Omega = \boldsymbol{V} + \nabla_{\boldsymbol{k}}\omega_r \tag{3.4}$$

for which $\boldsymbol{x} = (x, y, z)$ defines the domain space, $\nabla_{\boldsymbol{k}} = (\partial/\partial k,\ \partial/\partial l,\ \partial/\partial m)$ is the spectral gradient operator, and $\nabla_{\boldsymbol{k}}\omega_r$ defines the group velocity of a wave packet in a quiescent fluid. Equation 3.4 and the law governing wave refraction

$$\frac{d\boldsymbol{k}}{dt} = \nabla\Omega = -\boldsymbol{k}\cdot\nabla\boldsymbol{V} - \nabla\omega_r \tag{3.5}$$

are used to calculate the changes of the relative frequency with respect to time

$$\frac{d\omega_r}{dt} = \frac{d\boldsymbol{k}}{dt}\cdot\nabla_{\boldsymbol{k}}\omega_r + \frac{d\boldsymbol{x}}{dt}\cdot\nabla\omega_r \tag{3.6}$$

The first and second terms on the right-hand side of Equation 3.5 give, respectively, the wave refraction due to velocity gradients in the background flow and due to changes in fluid properties (e.g., N). However, the form of the dispersion relation selected for this research does not directly give ω_r as a function of $\boldsymbol{x}$, so the second term will be zero throughout this work.

Equations 3.3 through 3.5 with ω_r, found from either Equation 3.2 or 3.6, provide sufficient numerics for ray theory, but additional calculations are required to estimate the onset of nonlinearities. For example, wave overturning can be estimated using the vertical displacement of the fluid

$$\eta = \mathbb{R}\left[\eta_0 e^{-(z-z_0)^2/l_v^2} e^{i(\boldsymbol{k}\cdot\boldsymbol{x})}\right] \tag{3.7}$$

where the subscript 0 denotes a reference value and l_v is a vertical length scale. Ignoring the Gaussian term defining the packet size and differentiating with respect to z approximates wave steepness as

$$\frac{\partial\eta}{\partial z} \approx m\eta_0 \tag{3.8}$$

which can be understood physically as the slope of a wave.

η_0 is derived from the potential energy per unit volume of a wave packet averaged over a wave period, i.e., the wave energy density E_ρ. Given by Pedlosky [40], but adjusted here for the third dimension, the equation is

$$E_\rho = \frac{1}{2}\rho_0 w_0^2\left(\frac{k^2+l^2+m^2}{k^2+l^2}\right) \tag{3.9}$$

where $w_0 = \eta_0 \omega_r$ is the initial vertical velocity of the fluid and ρ_0 is a reference density. Rearranging and substituting Equation 3.2 into Equation 3.9 gives

$$E_\rho = \frac{1}{2}\rho_0 \eta_0^2 N^2 \left[1 + \left(\frac{fm}{N\sqrt{k^2+l^2}}\right)^2\right] \tag{3.10}$$

[29, 41–43].

Solving Equation 3.10 for η_0 and applying the mid-frequency approximation $(f << \omega_r << N)$ yields

$$\eta_0 \approx \left(\frac{2E_\rho}{\rho_0 N^2}\right)^{\frac{1}{2}} \tag{3.11}$$

Substituting into Equation 3.8 gives

$$\frac{\partial \eta}{\partial z} \approx \sqrt{(k^2+l^2)\frac{2A_\rho}{\rho_0 \omega_r}} \tag{3.12}$$

where $A_\rho = E_\rho/\omega_r$ is the wave action density [39].

Wave action A is a theoretical wave property first introduced to study property changes of a wave train [44]. It is conserved in time along a ray and is defined by the following integral

$$A = \int A_\rho \, d\forall \tag{3.13}$$

Assuming A_ρ is not a function of wave packet volume $\forall$, this equation becomes

$$A = A_\rho \forall = A_{\rho,0} \forall_0 \tag{3.14}$$

Values for the wave action density are typically not known a priori, but changes to the volume of a collection, or tube, of many tightly-arranged rays can be estimated using ray tube analysis [38]. This ray-tube volume approximates the volume of a wave packet. Thus, for purposes of calculation, Equation 3.14 can be rearranged such that a volume ratio $\forall_0/\forall$ replaces a wave action ratio $A_\rho/A_{\rho,0}$. Tracking changes in wave steepness is then facilitated by the ratio

$$\frac{\partial \eta/\partial z}{(\partial \eta/\partial z)_0} = \sqrt{\frac{k^2+l^2}{k_0^2+l_0^2}\frac{\forall_0}{\forall}\frac{\omega_{r,0}}{\omega_r}} \tag{3.15}$$

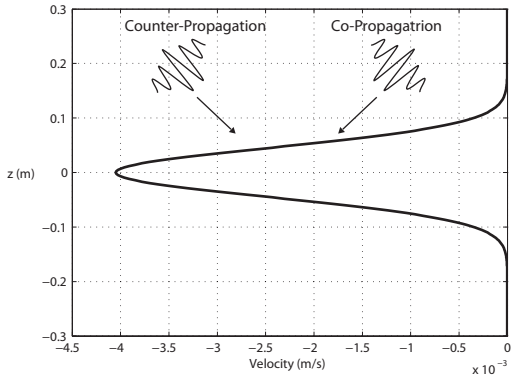

Figure 3.1: Packets of internal waves approach a two-dimensional steady shear from the same horizontal direction as the shear (co-propagation) and from the opposite horizontal direction as the shear (counter-propagation). Note the horizontal axis indicates the velocity of the shear and is not relative to the wave packets.

Changes in the total energy of a wave packet

$$E = \int E_\rho \, d\forall = \int A_\rho \, \omega_r \, d\forall \tag{3.16}$$

are also tracked. Assuming the integrand on the right-hand side is not a function of volume, the total energy simplifies to $E = A\omega_r$. Because ω_r may have the only known value here, it is best to take advantage again of the conservation of wave action and track the changes in energy with the ratio

$$\frac{E}{E_0} = \frac{A}{A_0}\frac{\omega_r}{\omega_{r,0}} = \frac{\omega_r}{\omega_{r,0}} \tag{3.17}$$

3.1.1 Interactions with a Two-Dimensional, Steady Shear Flow

This section explores the practice of ray theory, or ray tracing, as it tracks the wave refractions and changes to internal wave properties. To illustrate ray tracing, two internal wave interactions are considered as wave packets approach from different horizontal directions and interact with a two-dimensional steady shear. These will later serve as comparisons to the co- and counter-propagating wave-vortex dipole interactions along the vertical symmetry plane. Figure 3.1 shows these approaches schematically. The velocity profile of the shear is idealized with a Gaussian symmetrical about the depth $z = 0$ m. (Note that the horizontal axis measures velocity,

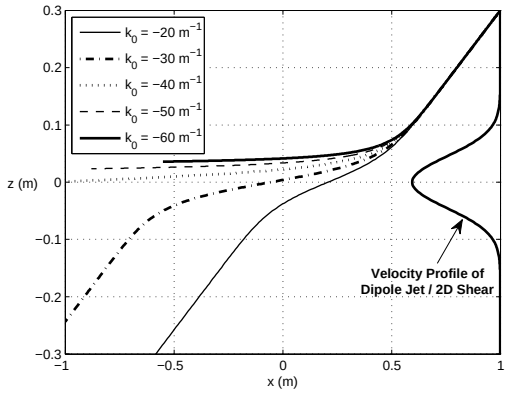

Figure 3.2: Each ray, co-propagating with the shear, is initiated from the same position and with the same relative frequency $\omega_{r,0} = 0.2$ s^{-1}, but with various initial horizontal wavenumbers. The velocity profile of Figure 3.1 is shown for reference at 100 times its magnitude.

applicable to the shear profile, but not to the internal wave packets, which are represented only spatially.)

Co-Propagating Interaction

Figure 3.2 demonstrates the qualitative output of two-dimensional ray tracing, which tracks the series of spatial positions of a wave packet for all time over the course of its simulated wave evolution. Internal wave packets co-propagating with the background shear are each given a different initial horizontal wavenumber and are initiated from the same position and with the same relative frequency $\omega_{r,0} = 0.2$ s^{-1}. The simulation for each of the packets was about 35 buoyancy periods. The paths, or rays, they traced during the interaction with the shear are shown. The various wave refractions, exhibited by the changing angles of propagation along each ray, are as distinct as the initial wavenumbers. The velocity profile is shown for reference at 10^2 times its magnitude.

Under certain conditions, such as for the rays with $k_0 = -20$ m^{-1} and $k_0 = -30$ m^{-1}, waves may exit the interaction with the final values of wave properties the same as the initial. This is quickly checked by observing that the angle of propagation below the shear is the same as that above the shear. For the other rays in Figure 3.2, internal wave interactions permanently alter the wave properties. The wave energy may be transferred to or dissipated by the background flow such that the waves no longer exist. Such an extreme case of wave energy loss occurs when in-

ternal waves approach a critical level. As the wave packet vertically propagates into the shear, the horizontal velocity experienced locally by the packet increases. Then, because the total frequency, defined in Equation 3.3, is a constant and the streamwise horizontal wavenumber k is unaltered by two-dimensional interactions, the relative frequency ω_r must decrease. The depth in the background flow at which, during the interaction, ω_r approaches its minimum possible value, the global rotational frequency of the medium (e.g., the Coriolis frequency in the case of a geostrophic flow, or zero if the medium is nonrotating), mathematically defines the depth of a critical level. At this critical frequency, internal waves cannot exist.

The simplest example of internal waves approaching a critical level is found in the wave interaction with a two-dimensional, steady shear flow in a non-rotating fluid of constant buoyancy frequency. Figure 3.3(a) shows the ray with initial horizontal wavenumber $k_0 = -60\ \mathrm{m}^{-1}$ asymptotically approaching a critical level z_c as time increases (measured in buoyancy periods). The changes to this ray's wave properties are displayed in Figures 3.3(b) through 3.3(d). As the packet enters the shear flow, the increasing local velocity gradient component $\partial U/\partial z$ of the background causes the vertical wavenumber m to increase per Equation 3.5 while the horizontal wavenumber k remains constant. Changes to the vertical wavenumber affect the vertical propagation of the wave packet as defined by the vertical component of the group velocity in Equation 3.4. Simplified for this two-dimensional, non-rotating interaction, the vertical group speed is

$$c_{g,z} = -\frac{Nkm}{\left(k^2+m^2\right)^{3/2}} \tag{3.18}$$

An increasing vertical wavenumber reduces the vertical group speed and causes the direction of wave packet propagation to asymptotically approach the horizontal. The earliest sign of wave refraction can be seen as the ray's slope begins to decrease near 10 buoyancy periods and approximately 0.11 meters above the Gaussian shear flow's symmetry line ($z = 0$ m). The slope steadily decreases for the remaining time of the simulation.

Internal waves definitively approach a critical level as the relative frequency approaches zero. Figure 3.3(b) shows the changes of the vertical wavenumber through time in buoyancy periods. It begins to increase at the same time that the refraction begins in Figure 3.3(a). If the initial vertical wavenumber is small enough or if the shear is strong enough, the vertical wavenumber will

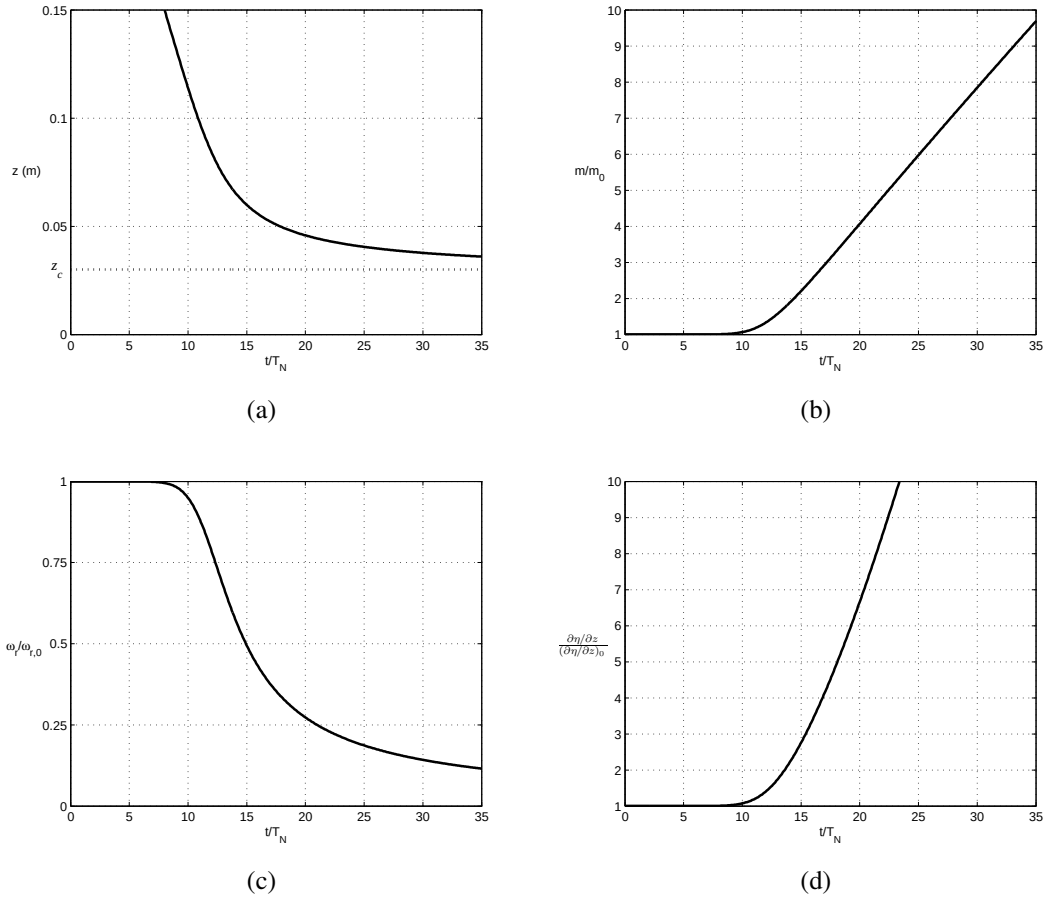

Figure 3.3: (3.3(a)) Temporal-depth plot of a ray approaching a critical level at depth $z_c \approx 0.03$ m. Corresponding changes to (3.3(b)) vertical wavenumber, (3.3(c)) relative frequency, and (3.3(d)) wave steepness.

increase sufficiently to cause the relative frequency to approach zero per the dispersion relation, simplified here for this two-dimensional, non-rotating interaction,

$$\omega_r^2 = \frac{N^2 k^2}{k^2 + m^2} \tag{3.19}$$

Figure 3.3(c) shows the changing relative frequency. With more time than shown, m approaches infinity and ω_r approaches zero, confirming the existence of a critical level.

Equation 3.17 shows that, due to the conservation of wave action, the ratio of relative frequency to its initial value is equivalent to the ratio of energy to initial energy. Thus, wave energy changes proportionally to relative frequency, decreasing with the relative frequency as the

waves approach a critical level. The resulting form of the energy is not always certain, but a couple of possibilities exist: the wave energy may be absorbed at the critical level, transferred to the background flow; or the waves may steepen, overturn and possibly break. The breaking of internal waves is similar to ocean surface waves crashing on a beach - the amplitude increases, steepening the waves enough that the greater-density fluid is directly above the lesser-density fluid, overturning the waves. If breaking ensues, the wave energy may dissipate through turbulence. Either way, continued wave propagation is unlikely.

Energy absorption and wave breaking are inherently nonlinear, thus linear ray theory cannot predict when or where they may occur, or even if they will. Wave steepness was introduced earlier as the slope of the waves and as one way to estimate the amount of overturning the internal waves experience. Where the initial steepness is unknown, the ratio of wave steepness to initial wave steepness is useful (Equation 3.15). The steepness ratio for the internal wave interaction with the two-dimensional, steady shear flow is given in Figure 3.3(d). Around 10 buoyancy periods, when the interaction begins to affect the waves, the steepness increases. It does so consistently, reaching a value one order of magnitude larger than its initial value before 25 buoyancy periods. Because overturning is estimated for values of wave steepness $\partial\eta/\partial z \geq 1$ [19], overturning and possible breaking would be expected of these internal waves if the initial steepness is large enough. Otherwise, one may anticipate absorption of the wave energy by the background at the critical level.

Counter-Propagating Interaction

In the case of counter-propagation (see Figure 3.1), the background shear may horizontally and vertically turn the wave propagation, as shown by the rays in Figure 3.4. As an extreme example, the ray with $k_0 = 70$ m is horizontally turned by the background so much that it reflects vertically. Another horizontal reflection follows, turning the wave packet again to its initial horizontal direction, completing a turning point.

Greater details of this interaction are provided in Figure 3.5. The interaction in time and depth is shown in Figure 3.5(a), where the changes in slope, or refractions, coincide with the property changes. As the wave packet propagates into the shear, the horizontal velocity experienced locally by the packet increases, though opposite in sign relative to the packet's horizontal propagation. The relative frequency ω_r must then increase because the total frequency defined in Equation

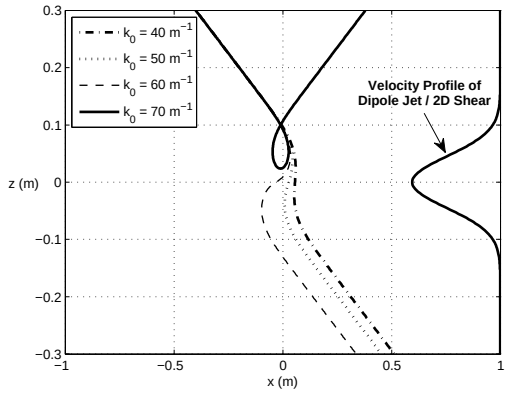

Figure 3.4: Ray tracing of four rays counter-propagating with a steady shear. Each is initiated from the same position and with the same relative frequency $\omega_{r,0} = 0.2$ s^{-1}, but with various initial horizontal wavenumbers. The velocity profile of Figure 3.1 is shown for reference at 100 times its magnitude.

3.3 is constant and the streamwise horizontal wavenumber k is unaffected during two-dimensional interactions, per Equation 3.4. Shown in Figure 3.5(b) and calculated from Equation 3.19, the relative frequency approaches its maximum possible value, the buoyancy frequency, as the vertical wavenumber, shown in Figure 3.5(c), changes sign. Resultantly, the vertical group speed also changes sign and the wave packet propagates upward (see Equation 3.18). The depth z_T at which this vertical reflection occurs is the turning point, defined by the relative frequency reaching the buoyancy frequency. At that instant, the wave steepness, shown in Figure 3.5(d), spikes to nearly six times its initial value. Again, ray theory does not yield results of the final state of the wave energy; so it is uncertain if this packet would overturn, though it is possible if given the right initial conditions.

3.2 Review of Experimental Setup

Godoy-Diana, et al. [25] completed the aforementioned experiments in a tank of linearly stratified saline solution. A columnar Lamb-Chaplygin vortex dipole was generated at one end of the tank by closing two flaps that spanned the tank's depth. The view was set such that the dipole translated right to left, as shown in Figure 3.6 (modified from Figures 1 and 2 of Godoy-Diana, et al. [25]). Downstream of the newly generated dipole a thin screen prevented all but a horizontal slice of the columnar dipole to pass into the interaction region of the tank, giving the pancake

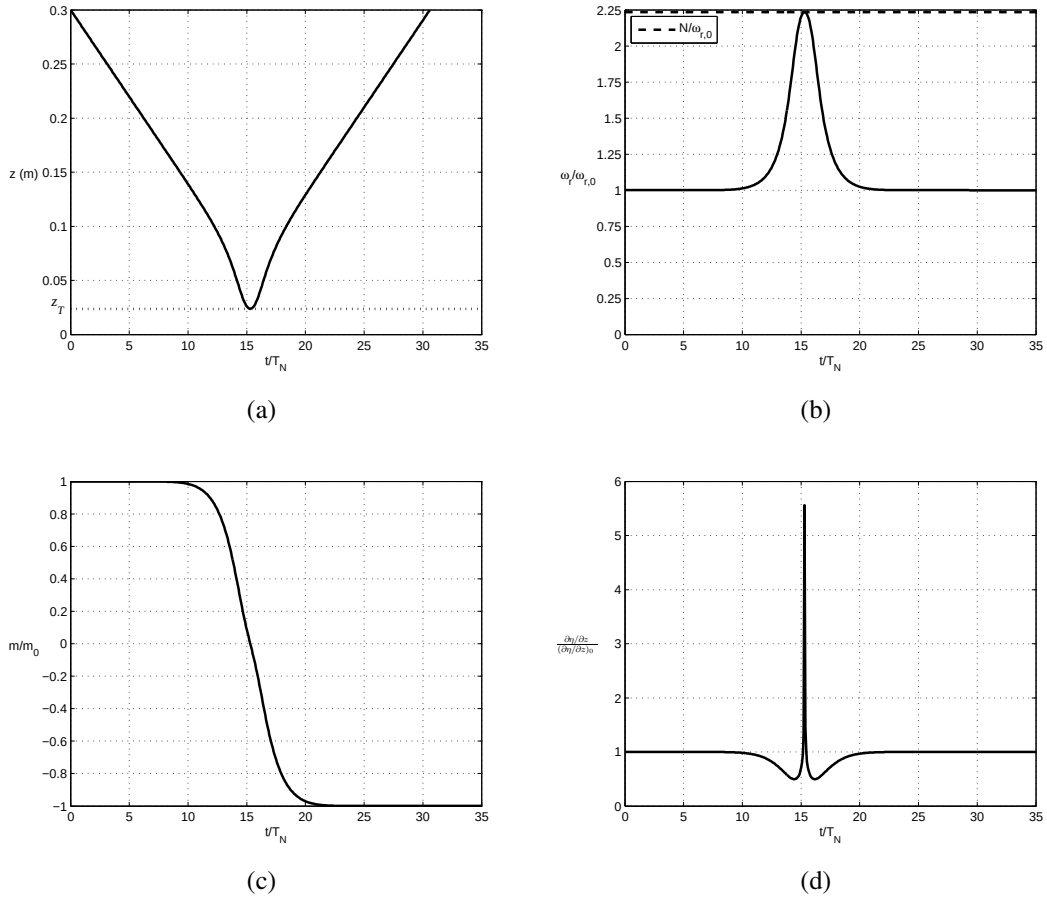

Figure 3.5: (3.5(a)) Temporal-depth plot of a ray experiencing a turning point at depth $z_T \approx 0.02$ m. Corresponding changes to (3.5(b)) vertical wavenumber, (3.5(c)) relative frequency, and (3.5(d)) wave steepness.

dipole an approximately Gaussian vertical distribution of velocity. The top half of this velocity profile is sketched in Figure 3.6. Above the interaction region of the experiments and spanning the width of the tank, a horizontal cylinder was oscillated to generate beams of internal waves. The translating dipole then intersected a beam, initiating an interaction (see also Figure 1.4(a)). As much as is possible, the results of this experiment are compared to the ray theory results presented in the next chapter.

3.3 Numerical Setup of Lamb-Chaplygin Vortex Dipole

Godoy-Diana, et al. [25] used three nondimensional control parameters to define the Lamb-Chaplygin pancake vortex dipole (named for two men who independently proved that its flow

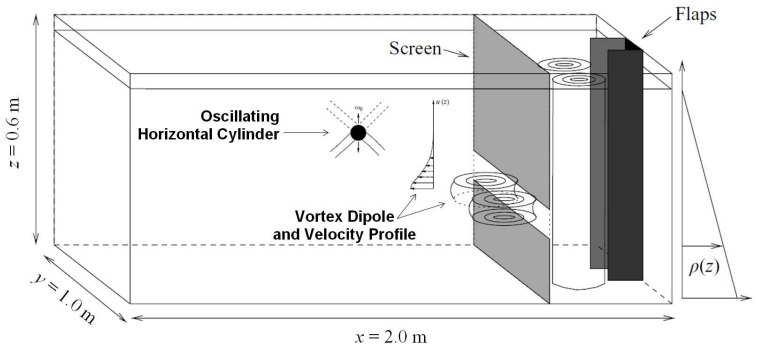

Figure 3.6: Schematic of the saltwater-stratified experimental tank (modified from Figures 1 and 2 of Godoy-Diana, et al. [25]). Two flaps at the right of the tank caused a columnar vortex dipole to translate leftward. From this, a screen formed a horizontal pancake vortex dipole and overlaid it with an approximately Gaussian vertical distribution of velocity, the top half of which is shown. Downstream, the pancake vortex dipole interacted with beams of internal waves being formed by one or more oscillating horizontal cylinders.

Table 3.1: Dipole Parameters and Properties

	Re	Fr_h	α	R (cm)	L_v (cm)	U_0 (cm/s)	N (s^{-1})	ν (m^2/s)
co-propagating	182	0.18	1.27	5.03	6.39	0.4	0.447	$1.12e^{-6}$
counter-propagating	131	0.06	0.40	7.40	2.96	0.2	0.447	$1.12e^{-6}$

satisfies the two-dimensional incompressible Euler equations [45]): the horizontal Froude number $\mathrm{Fr}_h = U_0/NR$, where U_0 is the translational speed of the dipole and R is the dipole radius; the Reynolds number $\mathrm{Re} = R^2 N \mathrm{Fr}_h/\nu$, where ν is the kinematic viscosity of the fluid; and the aspect ratio $\alpha = L_v/R$, where L_v is the vertical length scale of the dipole defined by a Gaussian envelope. Godoy-Diana, et al. [25] defined the values of these parameters for the experiments from which one can easily calculate R, L_v, and U_0. The values for all of these constants for each of the interaction cases are given in Table 3.1 (the value for the kinematic viscosity is assumed to be that of salt water and an experimentally-conducive value is assumed for buoyancy frequency).

The mechanics of the Lamb-Chaplygin vortex dipole were thoroughly described by Chaplygin [46], in which the equation of motion is the piecewise stream function in polar-coordinate

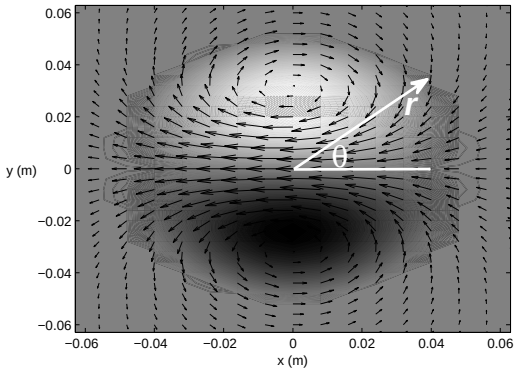

Figure 3.7: A top-down view of the numerically-simulated co-propagating vortex dipole at its horizontal midplane ($z = 0$ m). The light and dark contours represent positive and negative vorticity magnitudes, respectively, spanning approximately ± 0.8 s^{-1}. The vectors represent velocities, the strongest of which are located along the vertical symmetry plane ($y = 0$ m). Though velocity and vorticity magnitudes are different for the counter-propagating dipole, the flow is visually identical.

notation

$$\psi_0(r,\theta) = \begin{cases} -\dfrac{2U_0R}{\mu_1 J_0(\mu_1)} J_1\left(\mu_1 \dfrac{r}{R}\right)\sin\theta, & r \le R \\ \\ -U_0 r\left(1-\dfrac{R^2}{r^2}\right)\sin\theta, & r > R \end{cases} \tag{3.20}$$

where J_0 and J_1 are, respectively, the zero- and first-order Bessel functions of the first kind; and $\mu_1 = 3.8317$ is the first zero of J_1. The sign in each piece of the function enables right-to-left translation of the numerically-simulated dipole in a rightward-positive coordinate system to facilitate result comparisons with Godoy-Diana, et al. [25]. The vertical velocity profile is numerically simulated as the product of the dipole's local velocity $U(r,\theta)$ and an exact Gaussian curve $e^{-(z/L_v)^2}$, where z is the domain's range of depth.

The physical structure at the horizontal midplane (i.e., $z = 0$ m) of the numerically-simulated dipole used in the co-propagating interactions is presented in Figure 3.7 with the center positioned at the origin. Light and dark contours represent, respectively, positive and negative vorticity and span an approximate range of ± 0.8 s^{-1}. Velocity vectors overlying the vorticity contours show the relative position of the vortex dipole. The strongest velocities, shown by the longest vectors, are found where the vortices merge to form the jet of the dipole in the vertical symmetry plane (i.e., $y = 0$ m).

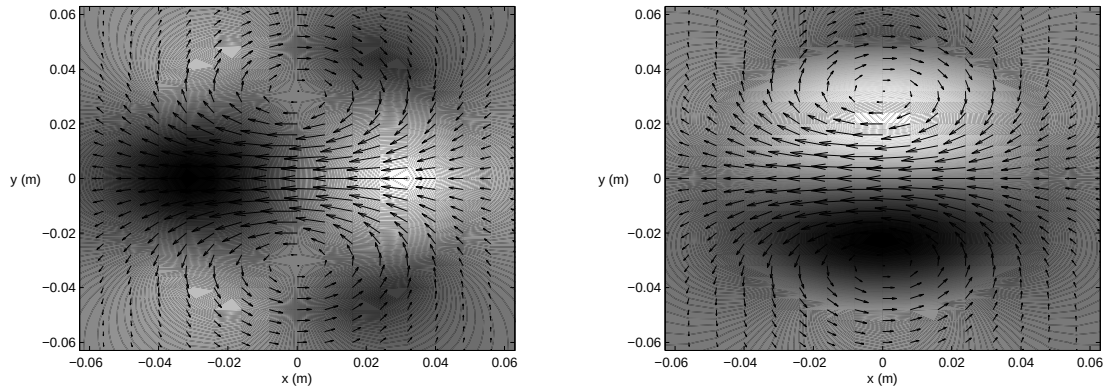

(a) $\partial U/\partial x$ (b) $\partial U/\partial y$

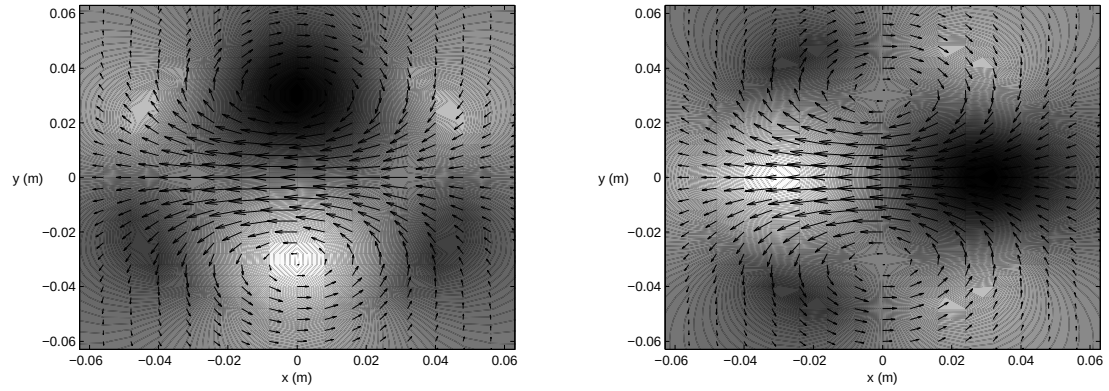

(c) $\partial V/\partial x$ (d) $\partial V/\partial y$

Figure 3.8: Horizontal velocity gradients of the co-propagating dipole at the horizontal midplane are given as light (positive) and dark (negative) contours. Velocity vectors overlie the contours to visualize the dipole's relative position. The dipole in the counter-propagating interactions has a visually identical flow though velocity magnitudes are different.

Figure 3.8 displays the local horizontal velocity gradients of the co-propagating dipole at the horizontal midplane as contours with the dipole's velocity vectors overlaid to give the relative position of the dipole. As in Figure 3.7, light contours are positive and dark contours are negative. The contours in Figure 3.8(b) have a range of about ± 0.6 m/s^2 and the others have an approximate range of ± 0.25 m/s^2 (the difference was for aesthetic purposes and so that the contours are visible in each frame). Though vorticity and velocity magnitudes are different for the dipole in the counter-propagating interactions, the flow is visually identical and Figures 3.7 and 3.8 can be referenced in discussions specific to both co-and counter-propagating interactions.

CHAPTER 4. RESULTS

The increased qualitative and quantitative awareness offered by the three-dimensional ray tracing assists in explaining certain phenomena not clearly seen or understood by the experiment alone, including focusing and defocusing outside of the vertical symmetry plane. Chapter 4.1.1 presents ray tracing results for co-propagating internal wave interactions with the dipole jet in the vertical symmetry plane. These are compared and contrasted with the experimental results and with ray tracings of an internal wave interacting with a two-dimensional steady shear flow (Chapter 3.1.1). The possibilities of critical levels and wave capture are discussed. In Chapter 4.1.2, ray theory solutions are presented for the co-propagating interactions away from the vertical symmetry plane, for which wave trapping is possible. Circumstances surrounding focusing and defocusing are discussed. Chapter 4.2.1 details ray tracings in the vertical symmetry plane of counter-propagating internal wave-vortex dipole interactions. A range of interactions are discussed, which include wave capture and turning points. The latter is compared and contrasted with the experimental results and to ray tracings of an internal wave interacting with a two-dimensional steady shear flow (Chapter 3.1.1). Chapter 4.2.2 focuses on rays traced outside the vertical symmetry plane and the corresponding focusing and defocusing.

4.1 Co-Propagating Interactions

4.1.1 Co-Propagating Internal Wave-Vortex Dipole Jet Interactions

The series of two-dimensional PIV images in Figure 4.1 shows the evolution of co-propagating internal wave-vortex dipole interactions observed in the vertical symmetry plane during the experiment (the complete series of images is found in Figure 9 of Godoy-Diana, et al. [25]). Above and to the right of the images, a horizontal cylinder was oscillated to generate the wave beams seen in the figure as diagonal lines. The direction of the wave energy propagation is along the beams, away

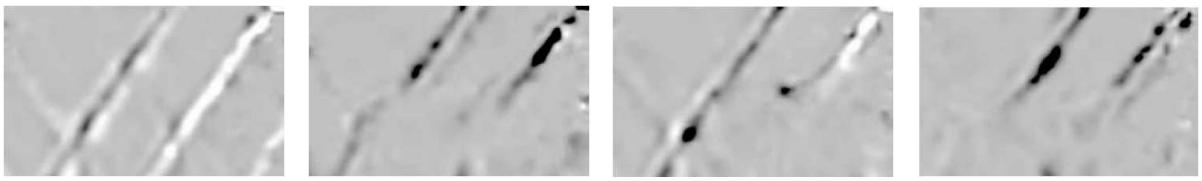

(a) t_1 (b) $t_1 + 28$ s (c) $t_1 + 39$ s (d) $t_1 + 53$ s

Figure 4.1: A series of two-dimensional PIV images showing the evolution of co-propagating internal wave beam-vortex dipole interactions as viewed in the vertical symmetry plane. The complete series of images is found in Figure 9 of Godoy-Diana, et al. [25].

from the cylinder. The black and white shading within each beam shows the phases of the internal waves. Figure 4.1(a) shows three undisturbed beams before the interaction began. In Figure 4.1(b), 28 seconds after the picture in 4.1(a) was taken, the beam in the lower right corner has sufficiently interacted with the dipole jet to have disappeared entirely from view, its energy absorbed by the jet. The middle beam can be seen bending to the horizontal as it interacts with the front of the dipole jet. After another 11 seconds, Figure 4.1(c) shows the dipole jet has absorbed the wave energy of the middle beam that was within its reach and is begining to absorb the wave energy of the left beam. In Figure 4.1(d), 14 more seconds have passed and the only remaining portions of the beams were above the influence of the dipole.

The initial conditions of the experiment are used in the ray tracing. The initial relative frequency was $\omega_{r,0} = 0.2$ s^{-1}. Godoy-Diana, et al. [25] provided a spectrum for the initial streamwise horizontal wavenumber used. A value near the end of this spectrum, $k_0 = -60$ m^{-1}, provides numerical results most similar to those of the experiment. Because the wave beams did not initially propagate in the spanwise direction, the initial horizontal spanwise wavenumber is $l_0 = 0$ m^{-1}. The initial vertical wavenumber is calculated from Equation 3.2 to be approximately $m_0 = 120$ m^{-1}. The components of the wavenumber vector are reevaluated at each time step and Equation 3.4 is integrated to solve for ω_r. The duration of each simulation is sufficiently long to ensure completion of the interaction (500 seconds, or approximately 35 buoyancy periods).

Positioning of the internal wave beams relative to the dipole were not provided by Godoy-Diana, et al. [25], so rays were somewhat arbitrarily initiated along x in the vertical symmetry plane and the dipole core was initiated at $x = 1$ m. Rays initiated between $x = 0.7$ m and $x = 0.85$ m interact with the jet of the dipole and bend to the horizontal similarly to the wave beams in Figure

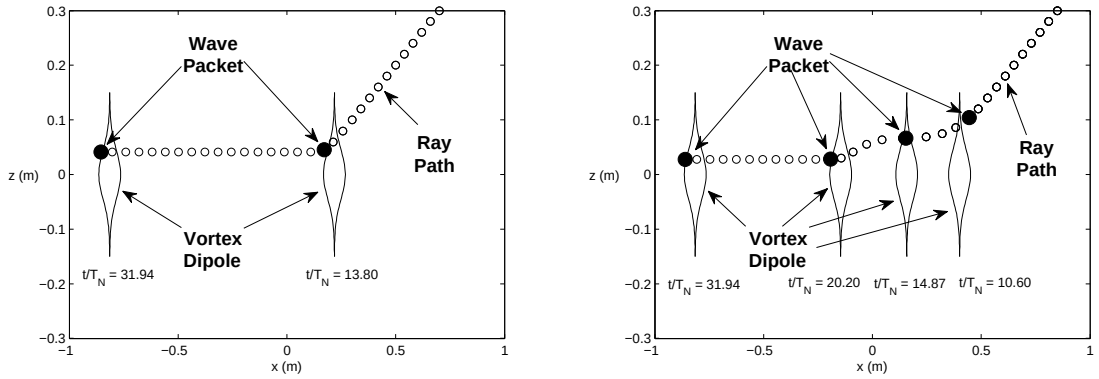

(a) (b)

Figure 4.2: Ray tracing, depicted by the circles, of the (4.2(a)) "Dipole Front" $(x_0 = 0.7 \text{ m})$ and (4.2(b)) "Dipole rear" $(x_0 = 0.85 \text{ m})$ interactions along the vertical symmetry plane. A filled circle indicates the location of a packet relative to the vortex dipole (the nearest profile sketch) at the labeled time.

4.1. The ray at each end of this range was selected for comparison because of the insight they offer into the mechanics of internal wave-dipole jet interactions. However, because the initial positions of the horizontal cylinder or wave beams and the dipole are unknown for the experiment, exact validation of the results of these rays is unfortunately impossible.

The ray of the first case is inititated at $x = 0.7$ m. A time series of snapshots is displayed in Figure 4.2(a). The circles follow the path traced by the packet in time during the interaction. A filled circle indicates the location of the wave packet relative to the vortex dipole (the nearest profile sketch) at the labeled time in buoyancy periods. The series shows that this interaction occurs in the streamwise decelerating region at the front of the dipole because the dipole overtakes the wave packet in the negative x-direction (compare Figure 3.8(a)). For that reason, this case is hereafter referenced as the "Dipole Front" interaction. Like the wave beams in Figure 4.1, the direction of wave propagation bends to the horizontal near the end of the fourteenth buoyancy period. The wave packet remains at the front of the dipole jet at an approximate depth of $z = 0.041$ m for the remainder of the simulation and the group speed reaches the dipole's translational speed.

The time series of snapshots for the second interaction, for which the packet is initiated at $x = 0.85$ m, is displayed in Figure 4.2(b). Around time $t/T_N = 10.60$ this packet enters the dipole at the rear and interacts in the streamwise accelerating region (see also Figure 3.8(a) along $y = 0$ m), so this interaction is hereafter referenced as the "Dipole Rear" interaction. A brief refraction

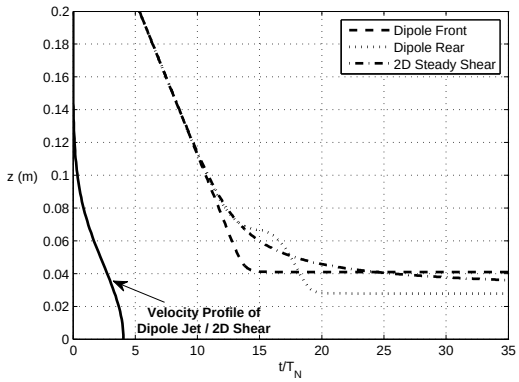

Figure 4.3: Co-propagating rays interacting along the vertical symmetry plane of the vortex dipole and with a two-dimensional steady shear. The backgrounds have similar velocity profiles. The steady shear is shown $1,000$ times its magnitude to reference its shape and vertical position relative to the rays.

decreases the vertical propagation of the packet for about four buoyancy periods, accelerating it to the front of the dipole at an approximate depth of $z = 0.067$ m. Then, before the vertical propagation reaches zero, a second refraction causes the packet to descend again, though not as steeply as during the initial approach to the interaction. The packet descends deeper into the dipole until refracting a third time around time $t/T_N = 20.20$, bending to the horizontal like the "Dipole Front" ray and in the experiment. Reaching a depth of about $z = 0.028$ m, the wave packet remains at the front of the dipole until the end of the simulation, its group speed equal to the translational speed of the dipole.

The rays of the above interactions are plotted together in the temporal-depth plot of Figure 4.3. In bending to the horizontal, these rays resemble those of internal waves approaching critical levels in two-dimensional steady shear flows, such as is traced by the ray labeled "2D Steady Shear." The initial wave properties of this ray are the same as for the "Dipole Front" and "Dipole Rear" rays. The initial streamwise position is inconsequential because the result is the same as long as it begins above the steady shear flow. It is natural to compare these because interactions along the vertical symmetry plane of the dipole are essentially two-dimensional. The only difference is the background flow. The velocity profile of the two-dimensional steady shear used the translational speed of the dipole to define the steady shear and is displayed at 10^3 times its magnitude to show its shape and position relative to the rays and their refractions.

Because $V = 0$ m/s in the dipole jet and $W = 0$ m/s everywhere in the domain, Equation 3.5 takes on a two-dimensional simplification,

$$\begin{aligned} \frac{dk}{dt} &= -k\frac{\partial U}{\partial x} \\ \frac{dl}{dt} &= 0 \\ \frac{dm}{dt} &= -k\frac{\partial U}{\partial z} \end{aligned} \tag{4.1}$$

where $\partial U/\partial x$ is the streamwise component of the velocity gradient of the dipole in the streamwise direction (see Figure 3.8(a)) and $\partial U/\partial z$ is the vertical shear of the dipole induced by the Gaussian envelope. Then, because $l_0 = 0$ m^{-1}, Equation 3.2 also simplifies for rays interacting with the dipole jet:

$$\omega_r^2 = \frac{N^2 k^2}{k^2 + m^2} \tag{4.2}$$

These are the same ray equations used for the "2D Steady Shear" ray.

Chapter 3.1.1 presented the topic of critical levels by discussing details of the "2D Steady Shear" interaction. There it was also discussed that the confirmation of a critical level requires the tracking of wave properties, since an approach to a critical level is defined by the relative frequency approaching zero. The following will similarly discuss the evolution of wave properties during the "Dipole Front" and "Dipole Rear" interactions, comparing and contrasting the properties with those resultant of the "2D Steady Shear" interaction. Although like properties of the various rays group together in the following figures so to facilitate comparisons between the different interactions, each interaction will be discussed one at a time.

To briefly repeat Chapter 3.1.1, in a two-dimensional steady shear, $\partial U/\partial x = 0$ so that the value of k is constant for any interacting rays (Equation 4.1). However, because $\partial U/\partial z$ increases as the waves propagate into the shear, the vertical wavenumber m changes. Approaching infinity, m causes ω_r to asymptotically approach zero and the internal waves approach a critical level (review Figures 3.3(b) and 3.3(c)).

In the vertical symmetry plane of the dipole, $\partial U/\partial x \neq 0$ and the wave mechanics are very different. As seen in Figure 4.4(a) and confirmed at $y = 0$ m in Figure 3.8(a), $\partial U/\partial x$ is strongly negative in the region where the "Dipole Front" ray enters the dipole because energy of the

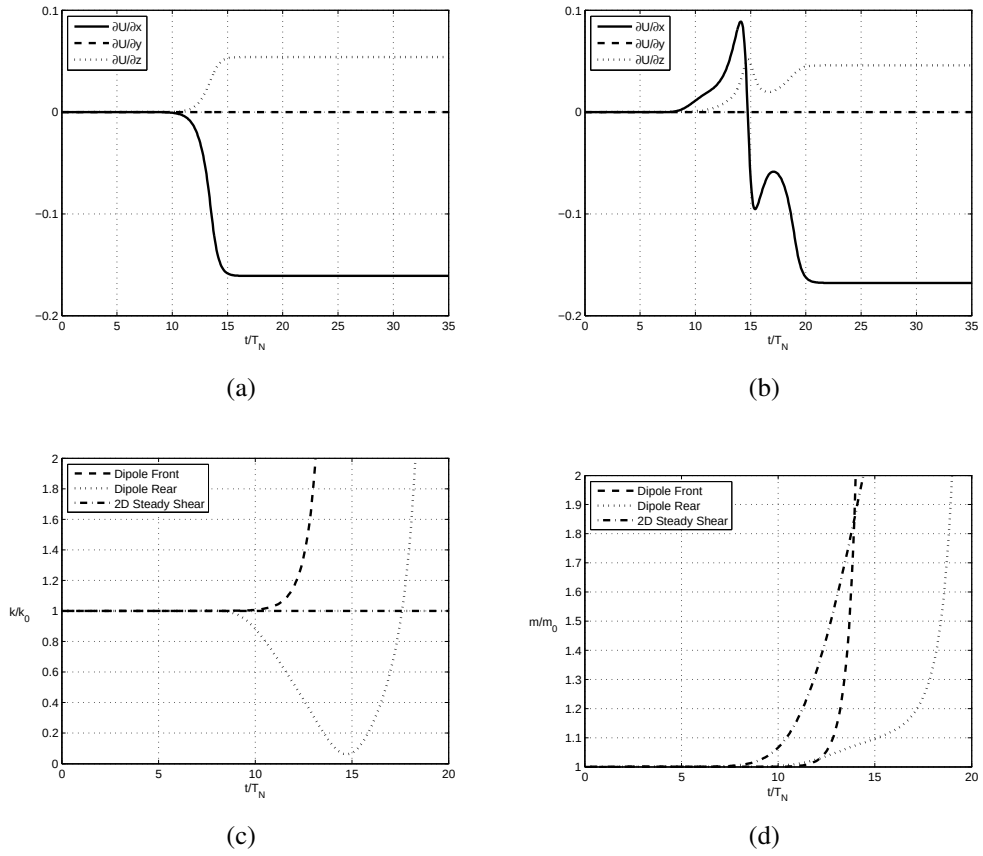

Figure 4.4: Dipole velocity gradients experienced locally by the wave packets during (4.4(a)) the "Dipole Front" and (4.4(b)) the "Dipole Rear" interactions. (4.4(c)) Streamwise horizontal and (4.4(d)) vertical wavenumbers calculated during the "Dipole Front," "Dipole Rear," and "2D Steady Shear" interactions.

dipole jet is transitioning to spanwise motions outside of the jet (i.e., $|V|$ increases as U decreases). The changes to the local dipole velocity gradients alter the streamwise horizontal and vertical wavenumbers of the "Dipole Front" ray according to Equation 4.1; curves for these wavenumbers are shown in Figures 4.4(c) and 4.4(d), respectivly, but only for the first 20 buoyancy periods since the curves approach infinity by this time. The spanwise wavenumber is not plotted because it does not change for interactions along the vertical symmetry plane. Because k grows negatively and $\partial U/\partial z$ increases positively, m increases. These property changes lead to the strong refraction at about $t/T_N = 13.80$ for which the ray is bending to the horizontal, though less gradually than does the "2D Steady Shear" ray approaching the critical level.

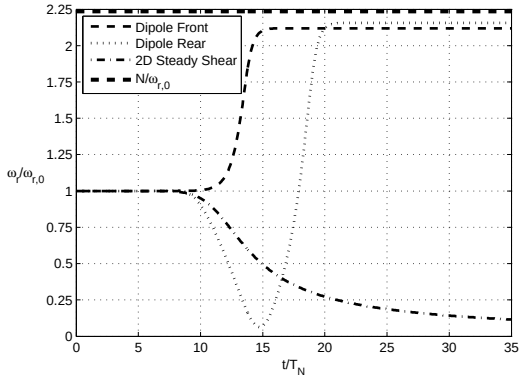

Figure 4.5: Relative frequency for the rays traced in Figure 4.3. The "2D Steady Shear" ray approaches a classical critical level, defined by the relative frequency asymptotically approaching zero. The "Dipole Rear" ray also does, but only temporarily. With increasing ω_r, the interactions with the dipole jet experience wave capture.

As each wavenumber increases exponentially, the numerator and denominator of Equation 4.2 balance in such a way that the relative frequency in Figure 4.5, after sharply increasing, plateaus at $\omega_r/\omega_{r,0} = 2.12$, short of reaching the value of the fluid's buoyancy frequency. This unbounded growth of k and subsequent finite plateauing of ω_r leads to wave capture [27, 34]. During wave capture, the group velocity of the wave packet approaches the translational speed of the dipole and is literally caught and pushed along by the flow.

According to Figure 4.4(b), and confirmed at $y = 0$ m in Figure 3.8(a), the "Dipole Rear" ray first experiences a positive $\partial U/\partial x$, which has two effects. First, the magnitude of k begins decreasing, causing the initial descent of ω_r. As this happens, the ray appears to approach a critical level much like the "2D Steady Shear" ray. Second, the positive $\partial U/\partial x$ accelerates the wave packet to the front where it experiences a negative $\partial U/\partial x$ as did the "Dipole Front" ray. At this same time, the second of three refractions causes $|k|$ to grow quickly to infinity, driving ω_r to more than double its initial value. The vertical wavenumber, which was increasing only slowly at first, now approaches infinity and balances the effects of the unbounded k in Equation 4.2 such that the relative frequency plateaus at about $\omega_r/\omega_{r,0} = 2.16$, just greater than the final relative frequency of the "Dipole Front" ray but still less than the fluid's buoyancy frequency. With unbounded wavenumbers, this last refraction leads to wave capture as for the "Dipole Front" ray.

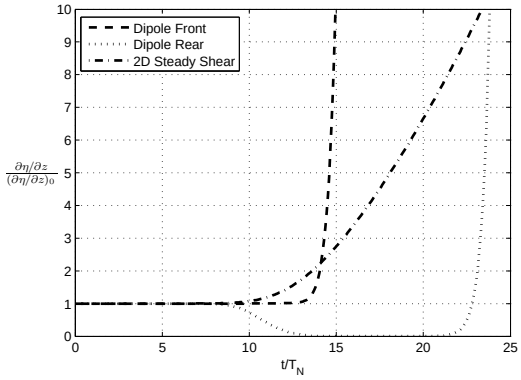

Figure 4.6: Wave steepness for the rays of Figure 4.3. As steepness increases, so does the possibility of wave overturning and breaking. In the case of the "Dipole Rear" interaction, the wave steepness first decreases, increasing the possibility of wave energy absorption as it first approaches a critical level.

Because the magnitudes of k and m approach infinity during these wave interactions with the dipole jet, the horizontal and vertical wavelengths decrease to zero and the waves should no longer exist. Though ray theory cannot predict the existence of the nonlinearities – wave energy absorption or wave breaking – that would cause this, the possibility of wave overturning can be investigated through wave steepness. Values of wave steepness $\partial\eta/\partial z \geq 1$ estimate overturning and imminent wave breaking [19], yet $\partial\eta/\partial z$ cannot be calculated exactly in this work because Equation 3.12 requires a known value for wave action density. As explained in Chapter 3.1, the best alternative is to apply the steepness ratio given in Equation 3.15. Figure 4.6 shows this ratio plotted as a function of time (only 25 buoyancy periods are shown because the steepness curves for each of the three interactions rapidly approach infinity). Because the steepness curve of the "2D Steady Shear" ray is unbounded, overturning is expected and wave breaking is possible. The increased steepness of the "Dipole Front" ray is similar, but wave breaking is not expected during wave capture [34]. However, the exponentially-increasing vertical wavenumber gives strong reason to believe overturning is possible [47]. Because wave capture is nonlinear [34], however, this study cannot confirm one or the other.

Wave breaking of the 'Dipole Rear" internal waves seems only possible if they are not first absorbed by the jet when $\partial\eta/\partial z$ is virtually zero. This wave dampening corresponds in time with the large decreases of $|k|$ and ω_r before $t/T_N = 15$, encouraging the likelihood of a critical level being located at the depth of this ray's first horizontal bending. The remaining question is

whether or not the dipole jet absorbs enough of the wave energy to prevent the packet from escaping the critical level, which is possible for internal waves in time-dependent backgrounds [47]. The subsequent increase in ω_r, E, and $d\eta/dz$ may then yield instabilities as might occur with the "Dipole Front" ray. However, this is contrary to research on wave capture [34].

Because the vortex dipole horizontally overtakes the wave packet of the "Dipole Front" interaction, it would seem that this interaction is most similar to the co-propagating experiment; but without the relative positioning of the wave beams and the dipole, validation is impossible. With known information, though, it may be argued that the wave bending to the horizontal reported by Godoy-Diana, et al. [25] is a result of wave capture and not of a critical level. When wave capture occurs, the wave energy exceeds two times its initial value and wave steepness increases infinitely, which may suggest subsequent wave breaking. This was clearly not observed during the experiment. However, because the wave beam in the experiment was continuously generated even as the dipole passed through it, the relative frequency and wave energy measured may have been later in the wave beam where it would have interacted with the rear of the dipole. If this was the case, the first refraction of the "Dipole Rear" ray shows that critical level interactions are possible. It may also be that breaking was not seen because wave capture does not allow it [34].

4.1.2 Co-Propagating Internal Wave-Vortex Dipole Interactions

Rays interacting with the dipole outside of the vertical symmetry plane experience spanwise velocities of the dipole and so refract in all three dimensions. Figures 4.7(a) and 4.7(b) show the "Dipole Front" and "Dipole Rear" interactions, respectively, for all time of the simulation and in the entire domain. Each shows eleven rays equally spaced spanwise across the domain from $y = -0.25$ m to $y = 0.25$ m, with the outermost rays nearly outside the influence of the vortices. Each ray was otherwise initiated at the same position in x and z, was given the same initial wave properties, and was simulated for the same duration of time as were the rays of the respective dipole jet interactions presented in Chapter 4.1.1. These figures are principally to show the entire domain and the relative positioning of the rays; they are not meant for critical analysis of the interactions.

Spanwise defocusing of the wave energy was seen in the co-propagating experiments [25]. The co-propagating ray tracings here give generally the same results, but with some variation. Temporal views of the spanwise horizontal refractions of rays initiated on the positive side of

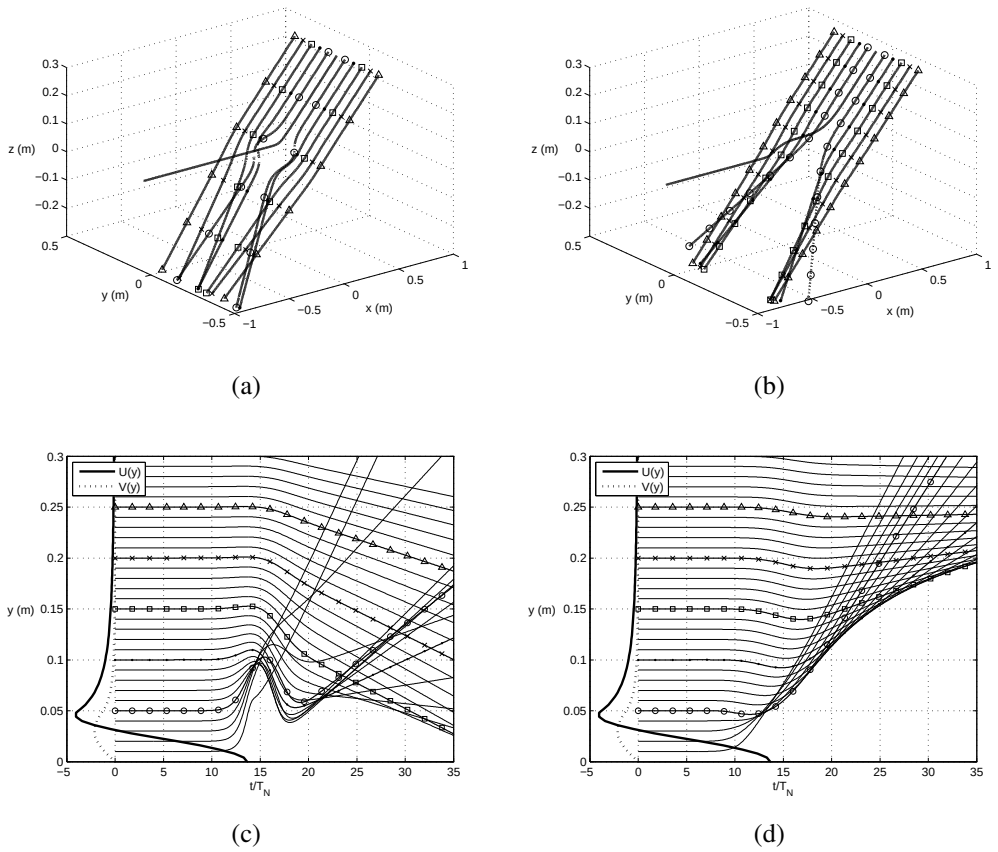

(a) (b)

(c) (d)

Figure 4.7: Three-dimensional ray tracings for the (4.7(a)) "Dipole Front" and (4.7(b)) "Dipole Rear" interactions. 4.7(c) and 4.7(d) show the spanwise refractions in time for each of these interactions, respectively. Focusing and defocusing are seen in 4.7(c) while defocusing is dominant in 4.7(d). The symbols on the rays in 4.7(c) and 4.7(d) correspond to the off-center rays in 4.7(a) and 4.7(b), respectively. Horizontal velocity profiles in 4.7(c) and 4.7(d) are magnified $1,000$ times to give spatial reference to the dipole.

the vertical symmetry plane are provided in Figures 4.7(c) and 4.7(d) for the "Dipole Front" and "Dipole Rear" interactions, respectively. The increased ray density provides a clear picture of focusing and defocusing. Those rays with symbols are the same rays displayed in Figures 4.7(a) and 4.7(b). The spanwise velocity profiles of U and V as they exist at the intersection of the horizontal midplane and the vertical plane spanning the cores of the vortices are displayed at 10^3 times their magnitudes to give their positions and shapes relative to the rays.

During the "Dipole Rear" interactions, the off-center rays principally defocus as expected based on the co-propagating experiment. But the ray tracing clearly shows that the spanwise refractions during the "Dipole Front" interactions vary depending on the initial position relative

to the dipole. Rays initiated at $y_0 > 0.11$ m actually focus while those initiated at $y_0 \leq 0.11$ m experience multiple spanwise refractions before ultimately defocusing. The available experimental data is given within a domain width approximately spanning $y = \pm 0.13$ m, so the outermost wave-vortex interactions may not have been easily observed in the experiment. Also, the collection data from a single horizontal plane may have made it impossible to see the detail of multiple refractions since they do not occur in a single plane.

Changes to wavenumbers of off-center rays are explained by the following simplification to Equation 3.5:

$$\begin{aligned} \frac{dk}{dt} &= -k\frac{\partial U}{\partial x} - l\frac{\partial V}{\partial x} \\ \frac{dl}{dt} &= -k\frac{\partial U}{\partial y} - l\frac{\partial V}{\partial y} \\ \frac{dm}{dt} &= -k\frac{\partial U}{\partial z} - l\frac{\partial V}{\partial z} \end{aligned} \tag{4.3}$$

where $\partial V/\partial x$ is the spanwise component of the dipole's velocity gradient in the streamwise direction (see Figure 3.8(c)), $\partial U/\partial y$ is the streamwise component of the dipole's velocity gradient in the spanwise direction (see Figure 3.8(b)), $\partial V/\partial y$ is the spanwise component of the dipole's velocity gradient in the spanwise direction (see Figure 3.8(d)), and $\partial V/\partial z$ is the spanwise component of the dipole's velocity gradient with respect to depth. To give an idea of what a single ray in each of these off-center interactions experiences in three dimensions, local velocity gradients of the dipole explaining the property changes of only the rays initiated at $y_0 = 0.05$ m are given in Figure 4.8. These curves show that rays outside of the vertical symmetry plane experience multiple local velocity gradients from many directions. These cause wave refractions in all directions, including multiple spanwise refractions in some cases.

Figure 4.9 exhibits the evolution of wavenumbers for the "Dipole Front" interactions. The curves shown represent only those rays inititated on the positive side of the vertical symmetry plane and are opposite in sign to their counterparts initated on the other side. In general, the curves of each wavenumber are similar to each other, especially those of k and m in Figures 4.9(a) and 4.9(c). The relatively small changes indicate only minimal refraction in the streamwise and vertical directions. However, in Figure 4.9(b) the curves marked by open and closed circles are

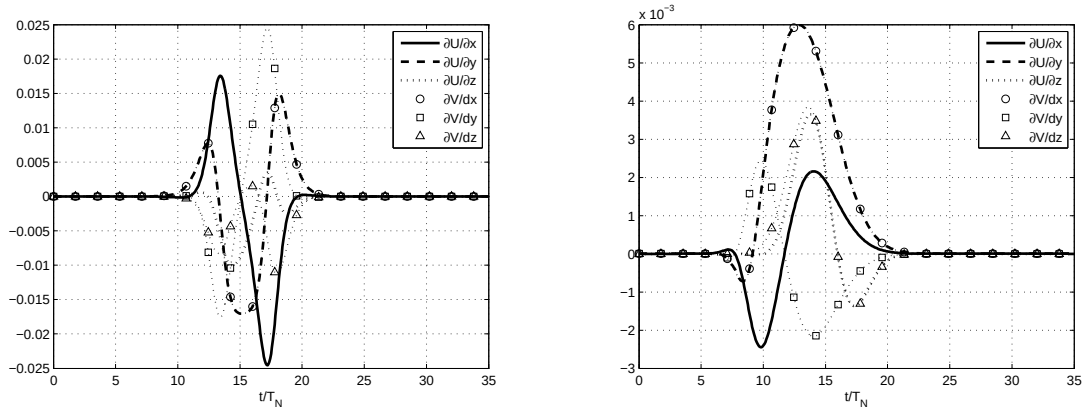

(a) (b)

Figure 4.8: Local dipole velocity gradients along the ray initiated at $y_0 = 0.05$ m during the (4.8(a)) "Dipole Front" and (4.8(b)) "Dipole Rear" interactions.

clearly different than the others. These curves correspond to rays in the "Dipole Front" interactions which experience multiple spanwise refractions before finally defocusing (hence the temporary volatility of l around $t/T_N = 15$). These refractions are resultant of the various extreme dipole velocity gradients experienced by these rays as they were nearest the vertical symmetry plane without interacting with the dipole jet. Moreover, rays experiencing multiple spanwise refractions close follow streamlines of a vortex in the frame of reference of the translating dipole. That is, they circle the core of the vortex until they escape the interaction, indicative of wave trapping. However, wave trapping has been shown to be a function of the vortex aspect ratio L_v/R [28], and efforts to show this for the type of wave-vortex interaction in the current study have thus far been unsuccessful.

The changes to the wavenumbers of the rays in the "Dipole Rear" interactions are shown in Figure 4.10. It may be noted that these rays experience similar changes in l, though the magnitudes are fairly different with those rays nearest the dipole jet having the greatest changes. These also initially experience increases in m as they more dramatically refract vertically.

In a three-dimensional, non-rotational frame of reference the dispersion relation simplifies to

$$\omega_r^2 = \frac{N^2\left(k^2+l^2\right)}{k^2+l^2+m^2} \tag{4.4}$$

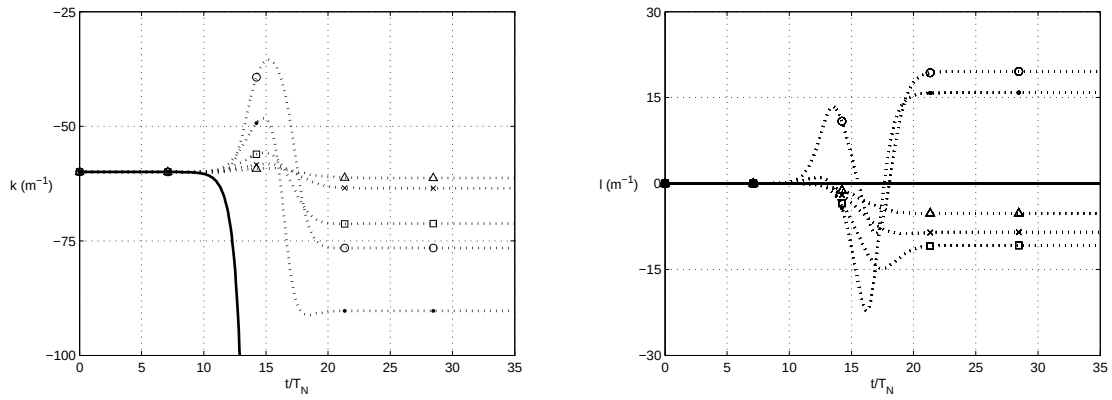

(a)

(b)

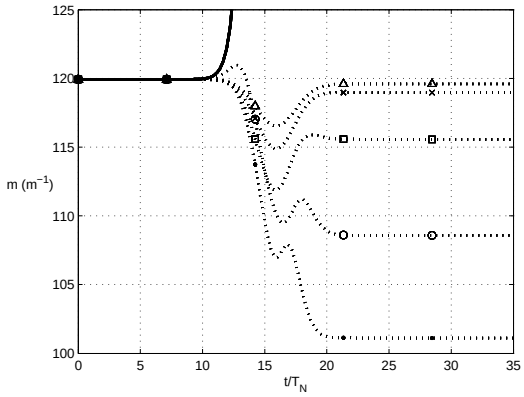

(c)

Figure 4.9: Wavenumbers for the off-center rays during the "Dipole Front" interactions. The symbols on the curves correspond to the rays on the positive side of the vertical symmetry plane in Figures 4.7(a) and 4.7(c). The thick, solid line is of the ray in the vertical symmetry plane, given for comparison.

Figure 4.11 shows the evolution of $\omega_r/\omega_{r,0}$ for each of the off-center rays (as well as that of the center ray for comparison) during the (a) "Dipole Front" and (b) "Dipole Rear" interactions. Due to the spanwise symmetry, each of the relative frequency curves associated with an off-center ray corresponds to two mirrored curves in either Figure 4.7(a) or Figure 4.7(b). Each of the "Dipole Front" rays experience similar changes to relative frequency, most of them decreasing somewhat before finishing the simulation at a higher relative frequency than initially and regardless whether the ray exited the interaction focusing or defocusing. The relative frequencies of the "Dipole Rear" rays likewise increase. Because $\omega_r/\omega_{r,0} = E/E_0$, these figures show that wave energy uniformly

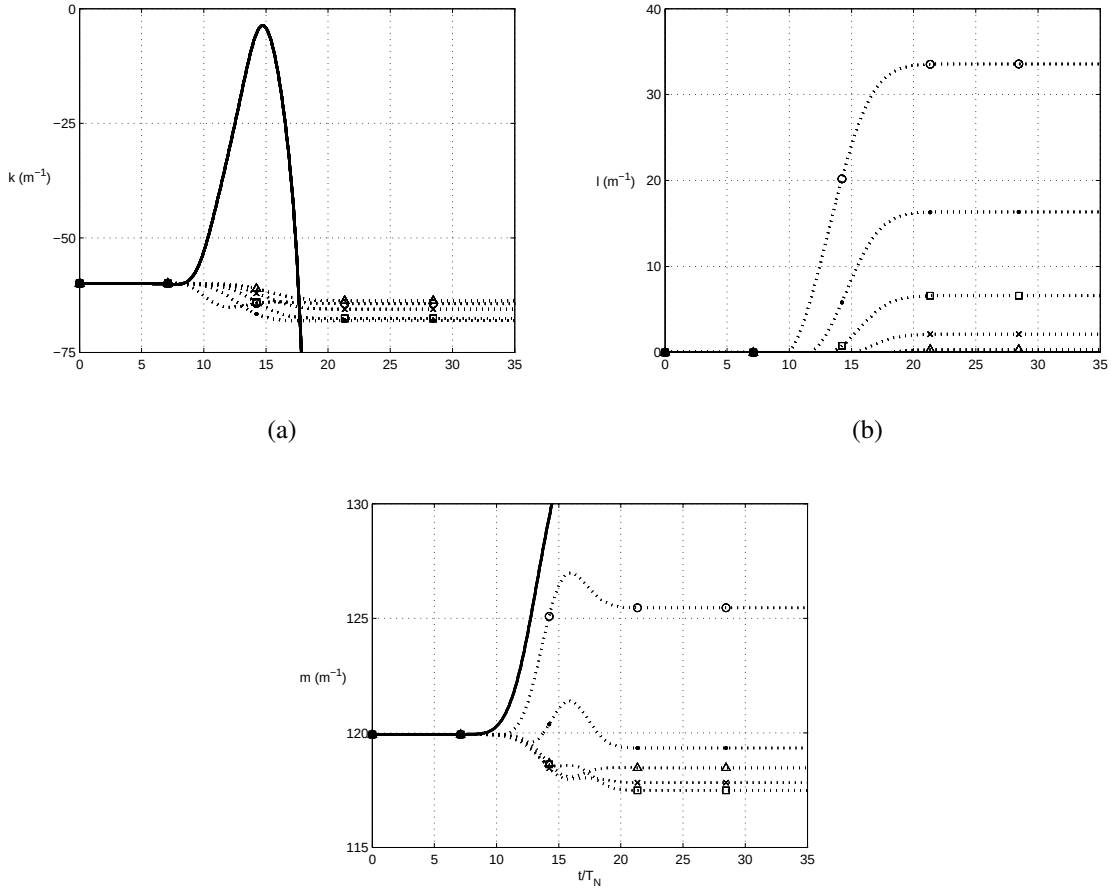

(a) (b)

(c)

Figure 4.10: Wavenumbers for the off-center rays during the "Dipole Rear" interactions. The symbols on the curves correspond to the rays on the positive side of the vertical symmetry plane in Figures 4.7(b) and 4.7(d). The thick, solid line is of the ray in the vertical symmetry plane, given for comparison.

increases for internal waves co-propagating with a vortex dipole. Exiting with greater energy, they may then have greater influence in later interactions.

Figure 4.12 shows curves of wave steepness for the (a) "Dipole Front" and (b) "Dipole Rear" interactions. Fluctuations in k, l, and ω_r are relatively small for off-center rays and do not greatly affect Equation 3.15, yet there are significant spikes in steepness. These occur at instances of strong wave refraction and are due to the wave packet volume suddenly approaching zero, indicative of wave amplitudes approaching infinity, a physical impossibility. These spikes in steepness are also of insignificant duration such that perhaps the extreme changes in magnitude are unrealistic, but they may also suggest the occurrence of nonlinearities, which may include break-

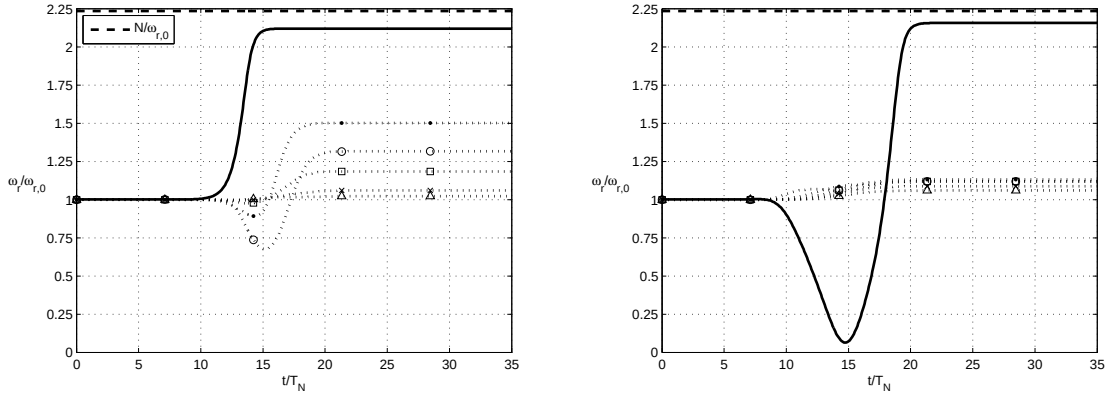

(a) (b)

Figure 4.11: Relative frequencies for the (a) "Dipole Front" and (b) "Dipole Rear" interactions. The symbols on the curves correspond to the rays in Figures 4.7(a) and 4.7(c) and Figures 4.7(b) and 4.7(d), respectively. The thick, solid line is of the ray in the vertical symmetry plane, given for comparison.

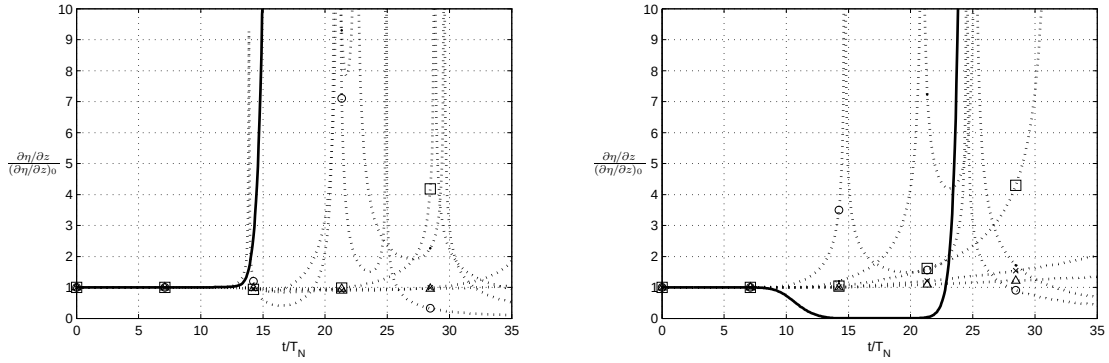

(a) (b)

Figure 4.12: Wave steepness for the (4.12(a)) "Dipole Front" and (4.12(b)) "Dipole Rear" interactions. The symbols on the curves correspond to the rays in Figures 4.7(a) and 4.7(c) and Figures 4.7(b) and 4.7(d), respectively. The thick, solid line is of the ray in the vertical symmetry plane, given for comparison.

ing. With overall increases to wave energy (per Equation 3.17) as well as steepness, it is possible that waves with even small initial wave steepness would eventually approach wave breaking.

The experiment showed that co-propagating interactions yield defocusing and should be the only expectation of spanwise refraction. The defocusing of the "Dipole Rear" rays shown in Figure 4.7(d) agrees with the experimental findings for co-propagating internal wave-vortex dipole

interactions [25]. The range of initial spanwise positions for defocusing "Dipole Front" rays in Figure 4.7(c) also agrees generally with the available experimental data for co-propagating interactions. Rays nearest the vertical symmetry plane defocus after experiencing multiple spanwise refractions, indicating probable wave trapping. Additionally, the "Dipole Front" interaction shows that focusing is possible for co-propagating rays initiated farther away from the vertical symmetry plane. The discussion thus far indicates that ultimately it is not the relative horizontal direction of interaction alone that determines whether focusing or defocusing will happen, but the initial properties and initial position of the internal waves relative to the dipole.

4.2 Counter-Propagating Interactions

4.2.1 Counter-Propagating Internal Wave-Vortex Dipole Jet Interactions

Godoy-Diana, et al. [25] reported the occurrence of a turning point in the vertical symmetry plane of the dipole when an internal wave beam of initial relative frequency $\omega_{r,0} = 0.2$ s^{-1} propagated counter to the directon of vortex dipole translation. Figure 4.13(a) provides a PIV image of this interaction from the experiment (for the complete series of images, see Figure 7a of Godoy-Diana, et al. [25]). The horizontal cylinder is located out of the view, above and to the left of the image. The internal wave beam is seen propagating down and to the right until it reaches a turning point. The reflected beam is seen propagating up and rightward. Wave energy is also seen well below the interaction. This is significant, and will be discussed at the end of this chapter.

Ray theory results from a range of initial positions mimic the counter-propagating experiment. Initiated at $z_0 = 0.3$ m and every five centimeters in the range $x_0 = [-0.1, 0.1]$ m, the five rays in Figure 4.13(b) demonstrate virtually the complete spectrum of possible results within the vertical symmetry plane. Though this spectrum of results can also occur by varying the initial relative frequency or wavenumber vector, the initial wave properties used here are the same as for the co-propagating interactions discussed above. The principal reason for doing this is that ray theory only realizes a turning point in the dipole jet for $k_0 \geq 60$ m^{-1} when $\omega_{r,0} = 0.2$ s^{-1}.

The ray initiated at $x_0 = 0.05$ m exhibits a turning point by looping its path in space over time. Though it appears dissimilar to that of the experiment, a loop is consistent with ray traced turning points that occur in a shear flow [11]. The sixth ray in Figure 4.13(b) shows such a turning

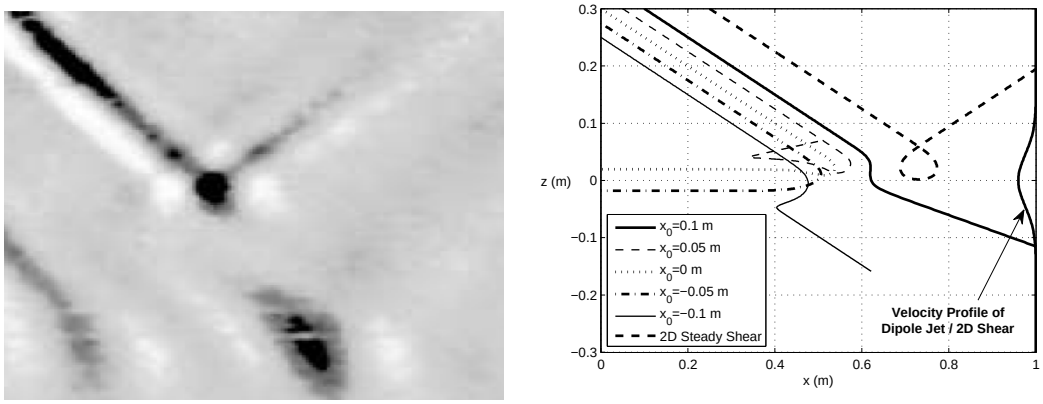

(a) (b)

Figure 4.13: (4.13(a)) PIV image showing an experimental counter-propagating internal wave-vortex interaction along the vertical symmetry plane of the vortex dipole. The complete series of images is found in Figure 7a of Godoy-Diana, et al. [25]. A turning point is seen as the internal wave beam reflects vertically. (4.13(b)) Temporal-depth plot of five rays in the vertical symmetry plane interacting with the counter-propagating vortex dipole jet. The sixth ray, labeled "2D Steady Shear" demonstrates a turning point in a steady shear and contrasts the turning point of the ray initiated at $x_0 = 0.05$ m. The velocity profile of the shear is also shown for reference at 10 times its magnitude.

point (discussed in Chapter 3.1.1). Labeled "2D Steady Shear," it simulates an interaction with a counter-propagating, two-dimensional steady shear, the same used earlier in the "2D Steady Shear" co-propagating example. The shear's velocity profile is defined by the translational speed of the dipole and is shown for spatial reference in Figure 4.13(b) at 10 times its magnitude.

Changes to relative frequency for the rays interacting with the dipole jet are calculated using Equation 4.2 and are displayed in Figure 4.14. Here, it is confirmed that the turning point definitively occurs at approximately $t/T_N = 15$ when the relative frequency approaches the buoyancy frequency. By this time, the dipole jet has already horizontally turned the wave packet. However, the horizontal wavenumber does not change sign (see Figure 4.15(a), so the leftward movement is entirely due to the dipole pushing the wave packet. Also, the horizontal and vertical wavenumbers (shown in Figure 4.15 and calculated using Equation 4.3) now quickly increase in magnitude as for the co-propagating rays in the vertical symmetry plane when they experience wave capture. The relative frequency sharply decreases as the wave packet expends its energy to propagate opposite the translation of the dipole and the negative $\partial U/\partial x$ in the jet (see Figure 4.15(c)).

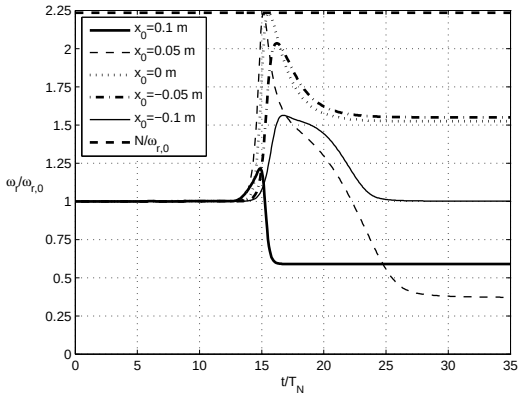

Figure 4.14: Changes of relative frequencies to the five rays interacting with the dipole jet in Figure 4.13(b).

At about $t/T_N = 22$, the ray passes the dipole's strongest velocities and enters the rear region of the dipole where it experiences positive $\partial U/\partial x$. Escaping wave capture, the ray now experiences a decreasing $\partial U/\partial z$ (Figure 4.15(d)) as it propagates upward. As $\partial U/\partial z$ approaches zero, the ray exits the dipole and slowly propagates rightward, as dictated by the positive horizontal wavenumber. The ray's continued propagation is in a quiescent medium. Thus the completion of the turning point does not happen while the wave packet is interacting with the dipole jet.

The lack of resemblance of the ray traced turning point to the shape and size of the turning point observed in the experiment may likely be due to the linear limitation of ray theory. That is, there may be non-linear mechanics, especially following the vertical reflection, which ray theory cannot predict. In fact, as will be discussed at the end of this chapter, a nonlinear effect of this interaction, called tunneling, causes a portion of the wave energy seen below the turning point and the dipole during the experiment. For the ray traced turning point, the wave energy of the packet increases more than 100% before the dipole jet absorbs more than half of the initial wave energy. The wave steepness, shown in Figure 4.16, increases steadily and quickly immediately following the vertical reflection. If the initial wave steepness is sufficient, then overturning – a nonlinear effect – is possible. However, as the ray leaves the interaction, the steepness rapidly decays. Even in the extended simulation, it never fully reaches zero; but, with only one-third the initial wave energy, it seems that the waves only barely survive the interaction and only if nonlinearities do not set in earlier. Assuming the waves do continue to exist, the group velocity decreases so greatly as

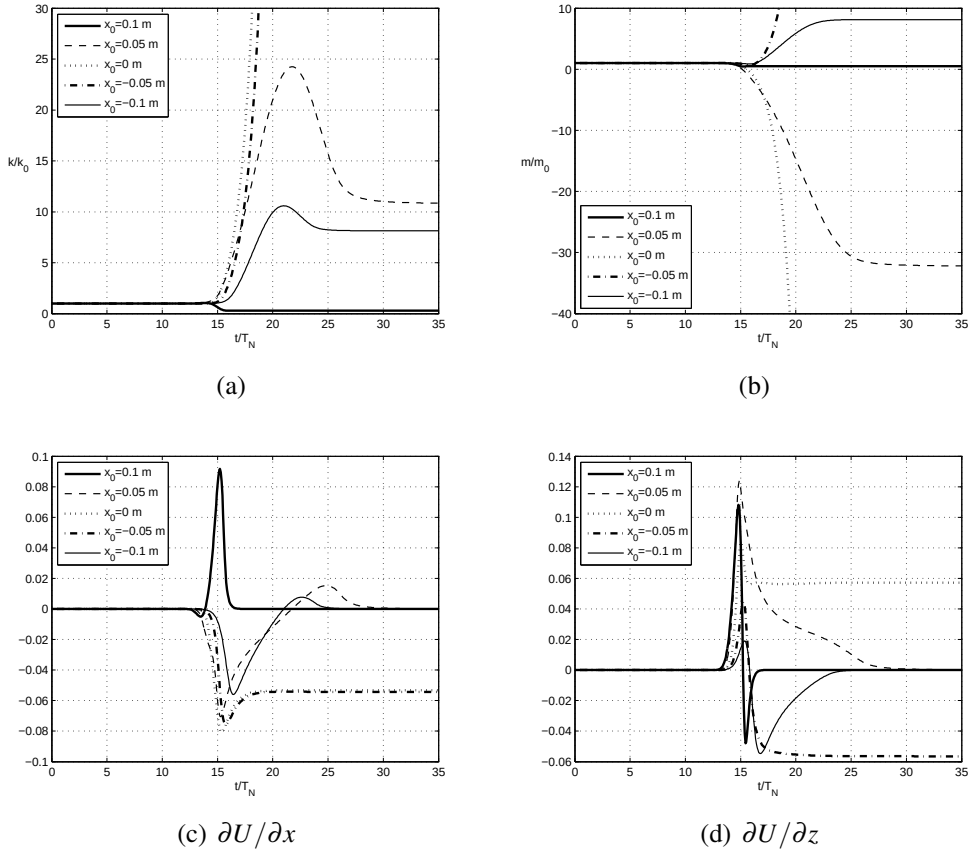

(a) (b)

(c) $\partial U/\partial x$ (d) $\partial U/\partial z$

Figure 4.15: Wavenumbers of and local dipole velocity gradients experienced by the five rays interacting with the dipole in Figure 4.13(b).

the waves exit the passing dipole that 142 additional buoyancy periods were required before the ray completes the loop of the turning point shown in Figure 4.13(b).

Returning to Figure 4.13(b), the rays initiated at $x_0 = 0$ m and $x_0 = -0.05$ m reflect horizontally and then experience wave mechanics like those experienced by the co-propagating "Dipole Front" and "Dipole Rear" rays in the vertical symmetry plane. The wavenumbers are unbounded, the relative frequencies plateau well above their initial values, the vertical group speeds asymptotically approach zero, and the horizontal group speeds approach the translational speed of the dipole. Indeed, these rays experience wave capture. They even experience a surge in amplitude as the wave steepness increases to infinity as it did during the co-propagating interactions. The ray initiated at $x_0 = 0$ m also experiences a vertical turning point which causes the vertical wavenumber to change sign and approach negative infinity before the ray plateaus a little above the horizontal midplane.

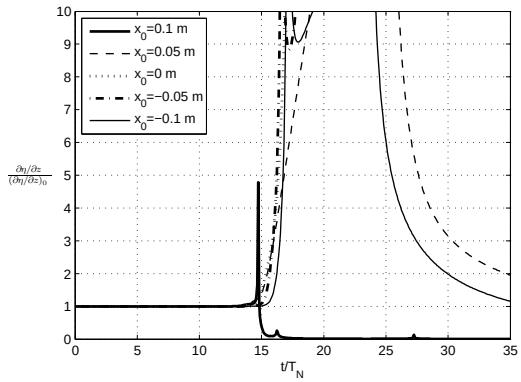

Figure 4.16: Changes to wave steepnesses of the five rays interacting with the dipole jet in Figure 4.13(b).

The corresponding change in sign of $\partial U/\partial z$ causes the positive exponential growth of the vertical wavenumber. The ray initiated at $x_0 = -0.05$ m does not reflect vertically and plateaus below the horizontal midplane of the dipole. It is expected that wave energy is transferred to the dipole flow [34].

Because they also enter the front of the dipole, each of the remaining rays initially interact with positive $\partial U/\partial x$ and experience an increasing horizontal wavenumber. One ray, intitiated at $x_0 = 0.1$ m, ultimately experiences a decrease in k because it passes briefly through the front of the dipole and then slows due to the positive $\partial U/\partial x$ in the rear. This short interaction is sufficient for the dipole to absorb nearly one-half the wave energy, which is enough to cause the steepness to become negligible for the majority of the simulation.

The ray initiated at $x_0 = -0.1$ m has many things in common with the ray just discussed. One difference of interest, though, is that the relative frequency approaches the initial value. Though it interacts with the dipole to a greater extent than the other ray, having shifted nearly 10 cm along the length of the domain, it ultimately experiences little to no energy exchange with the background and leaves the dipole at virtually the same angle of propagation at which it entered. Most of the cases of internal wave-vortex dipole interactions discussed to this point have shown an exchange of energy from the vortex dipole to the internal waves. This case also shows that the waves can also yield their energy to the dipole.

Counter-propagating rays in the vertical symmetry plane do not experience a uniform increase or decrease of wave energy. Rather, their final values of relative frequency nearly span the

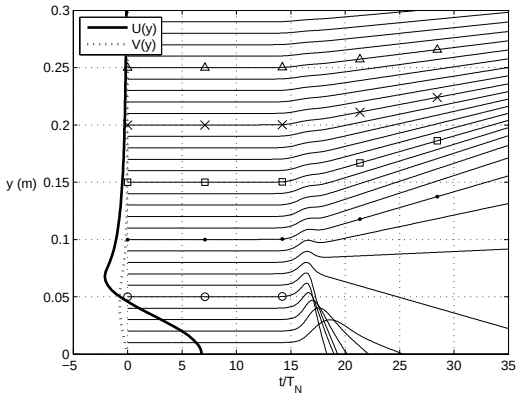

Figure 4.17: Temporal-width view of counter-propagating rays initiated at $x_0 = -0.1$ m. Focusing and defocusing are both possible. This was uniformly found for all counter-propagating interactions studied.

possible spectrum. Yet, nearly all have great increases of wave steepness, giving possibility to wave overturning and breaking. If the rays do not break or are not absorbed, then a variety of internal wave phenomena are possible, including turning points, as Godoy-Diana et al. [25] reported, and wave capture.

4.2.2 Counter-Propagating Internal Wave-Vortex Dipole Interactions

Figure 4.17 displays the spanwise refractions in time of rays initiated at $x_0 = -0.1$ m (for brevity, results of only this initial position will be presented). It shows that both focusing and defocusing are possible for a given set of initial wave properties and position. This is the general result found despite the value for x_0. The five rays marked with symbols are emphasized in the following figures.

The focusing predicted by ray theory for the rays in Figure 4.17 generally agrees with the experiment, but it is less severe for each ray traced farther outward until rays actually defocus. Defocusing was not reported for the experimental counter-propagating interactions, but the available experimental data does not extend to the outer spanwise boundaries [25]. The experiment also did not report the multiple spanwise refractions predicted by ray theory. Rays initiated at $y_0 \leq 0.07$ m, due to the rotation of the vortex, first defocus before sharply focusing, crossing their symmetric counterparts (not traced in the figure) at the vertical symmetry plane. However, as suggested be-

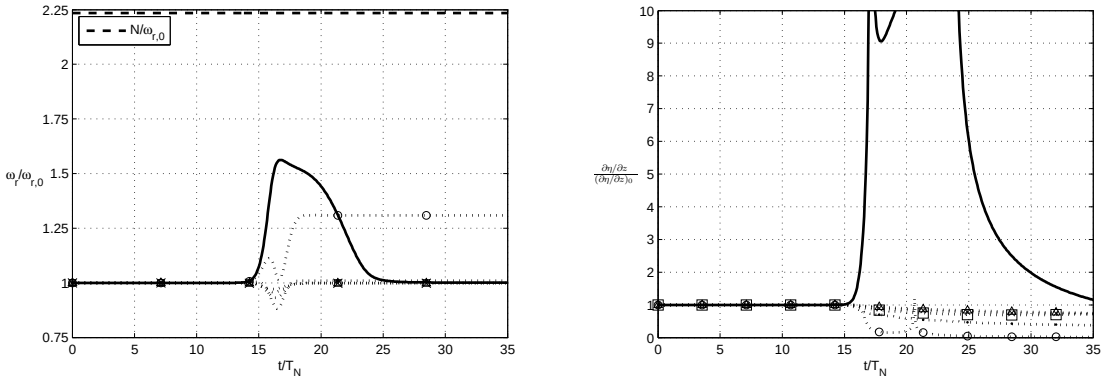

Figure 4.18: (4.18(a)) Relative frequency and (4.18(b)) wave steepness of counter-propagating rays initiated at $x_0 = -0.1$ m. The curves in either figure with symbols correspond to rays in Figure 4.17 and the thick solid curves corresponds to the ray in the vertical symmetry plane of the same interaction.

fore, the data collection of the experiment was limited to a single horizontal plane, which may have prevented clear viewing of all the refractions and corresponding details occurring in layers of the dipole above and below this plane.

Figures 4.18 through 4.19 display the changes in wave properties for the five highlighted rays and, for comparison, the ray in the vertical symmetry plane, represented by the thick, solid line. Only the focusing rays, i.e., those nearest the dipole jet, experience any real increase in relative frequency, and thus wave energy. The rest not only have minimal energy exchange with the dipole, but they also complete the interaction with virtually all the initial wave energy. It isn't a surprise, then, that all these rays experience very little change in wave steepness with those that focus experiencing the greatest decreases.

Godoy-Diana, et al. [25] showed that internal waves counter-propagating with a vortex dipole experience only focusing. However, their view was likely limited. This work has shown that internal waves interacting with a counter-propagating vortex dipole may focus and defocus, depending on initial wave properties and initial position relative to the dipole. Rays initiated nearest the vertical symmetry plane may experience wave trapping before focusing, while those initiated farther out defocus. Only rays within 5 cm of the vertical symmetry plane experience minor increases in wave energy, but they also experience the greatest relative decreases in wave steepness as

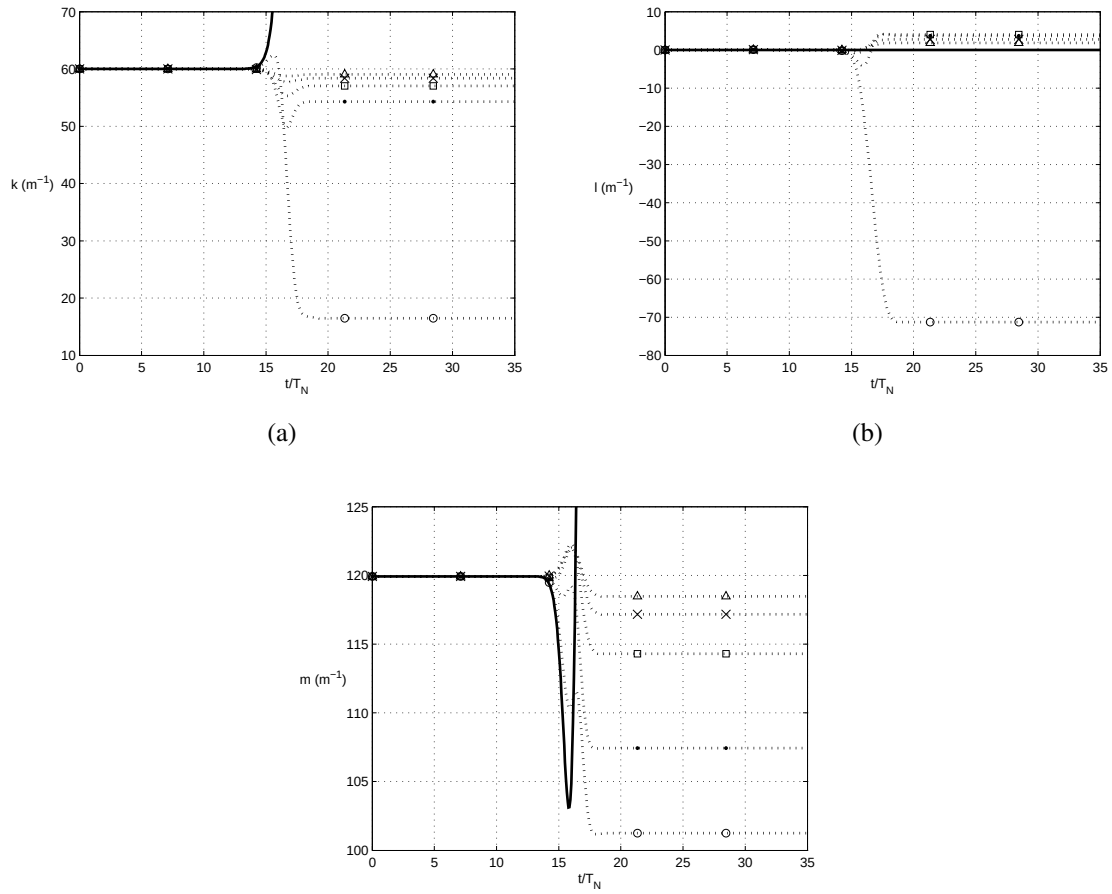

Figure 4.19: Wavenumbers of counter-propagating rays initiated at $x_0 = -0.1$ m. The curves with symbols correspond to rays in Figure 4.17 and the thick solid line corresponds to the ray in the vertical symmetry plane of the same. (Note: k and m for the ray in the vertical symmetry plane do not approach infinity (see Figures 4.15(a) and 4.15(b), respectively)).

they focus. With only marginal changes to these properties, the overall influence of this particular interaction is minimal.

With the three-dimensional effects of the counter-propagating interactions explained, especially focusing, a comment or two regarding the portion of wave energy seen below the turning point and the dipole in Figure 4.13(a) can be explained. On a second horizontal plane located at this depth, PIV measurements recorded transmission of wave energy through the dipole along the vertical symmetry plane instead of reflecting at the turning point [25]. Others studying this particular phenomenon call it tunneling [11]. Tunneling suggests that the stratification remains strong

throughout the layers of the dipole [48]. Because ray theory cannot predict tunneling, a nonlinear effect, it is not emphasized in this thesis.

The PIV measurements at this second horizontal plane also showed off-center-generated wave energy converging on the vertical symmetry plane [25]. All cases of counter-propagating ray tracing considered in this work agree with this finding. In the counter-propagating case initiated at $x_0 = 0.05$ m, for which the turning point occurs in the vertical symmetry plane, off-center rays focus and converge at the vertical symmetry plane at the same location relative to the turning point as is seen in the PIV image of the experiment. In crossing the vertical symmetry plane, focusing internal wave energy would interact with its symmetric counterpart. Such an intersection of wave energy would occur, of course, during the experiment, but the effects of this are not calculable using ray theory because each ray is independently traced. Therefore, this work has not considered the dynamics of the expected interaction.

CHAPTER 5. CONCLUSION

Godoy-Diana et al. [25] reported that, during interactions with a Lamb-Chaplygin pancake vortex dipole in the vertical symmetry plane of the dipole, internal wave beams approached critical levels when co-propagating with the dipole and turning points when counter-propagating. Outside of the vertical symmetry plane, spanwise spreading of wave energy was seen in the horizontal mid-plane of the dipole, defocusing during co-propagation and focusing during counter-propagation. The ray tracing of this work generally agrees with the available experimental data, but that data was collected from single, two-dimensional planes which were limited in their view of the interactions. Ray tracing agrees critical levels and turning points are possible, respectively, in co- and counter-propagating interactions; and, where ranges of initial spanwise ray positions match the views provided by the experiment, defocusing and focusing respectively correspond to co- and counter-propagating interactions. The location where waves enter the dipole jet plays a critical part in the final outcome of the waves since changes to the local accelerations experienced by the various rays cause wave properties to change in diverse ways. Table 5.1 summarizes the interactions discussed in this thesis.

Table 5.1: Summary of Internal Wave-Vortex Dipole Interactions Predicted by Ray Theory

	Critical Level	**Turning Point**	**Wave Capture**	**Wave Trapping**	**Focusing**	**Defocusing**
Co-Propagating						
Dipole Front, $x_0 = 0.7$ m			$y_0 = 0$ m		$\lvert y_0\rvert > 0.11$ m	$\lvert y_0\rvert \leq 0.11$ m
Dipole Rear, $x_0 = 0.85$ m	$y_0 = 0$ m (1^{st})		$y_0 = 0$ m (2^{nd})	$\lvert y_0\rvert \leq 0.11$ m		$\lvert y_0\rvert > 0$ m
Counter-Propagating						
$x_0 = -0.1$ m				$\lvert y_0\rvert \leq 0.07$ m	$\lvert y_0\rvert \leq 0.07$ m	$\lvert y_0\rvert > 0.07$ m
$x_0 = -0.05$ m		$y_0 = 0$ m		$\lvert y_0\rvert \leq 0.07$ m	$\lvert y_0\rvert \leq 0.07$ m	$\lvert y_0\rvert > 0.07$ m
$x_0 = 0$ m			$y_0 = 0$ m	$\lvert y_0\rvert \leq 0.07$ m**	$\lvert y_0\rvert \leq 0.09$ m	$\lvert y_0\rvert > 0.09$ m*
$x_0 = 0.05$ m			$y_0 = 0$ m	$\lvert y_0\rvert \leq 0.03$ m**	$\lvert y_0\rvert \leq 0.12$ m	$\lvert y_0\rvert > 0.12$ m
$x_0 = 0.1$ m					$\lvert y_0\rvert \leq 0.2$ m	$\lvert y_0\rvert > 0.2$ m

Initial conditions: $\omega_{r,0} = 0$ s^{-1}, $|k_0| = 60$ m^{-1}, $l_0 = 0$ m^{-1}, $m_0 = 120$ m^{-1}, $z_0 = 0.3$ m

*$|y_0| = [0.03, 0.04]$ m also defocused

**$|y_0| = \leq 0.02$ m show greatest evidence of wave trapping

Ray tracing also expands understanding of these interactions where the experiment may be limited. In the vertical symmetry plane and relative to the dipole, a range of initial positions (approximately $x_0 = 0.7$ m to $x_0 = 0.85$ m at $z_0 = 0.3$ m in this work) for rays co-propagating with the dipole yield results similar to critical levels, refracting to the horizontal as the vertical group speed approaches zero. However, the relative frequency does not approach zero. Some rays, especially those interacting with the front of the dipole, experience wave capture during which the relative frequency increases to values near the buoyancy frequency as the vertical and streamwise horizontal wavenumbers are unbounded and the horizontal group speed approaches the background translational speed. Rays that enter the dipole from behind may approach critical levels, but they may also escape the critical levels, accelerate to the front of the dipole, and experience wave capture.

When counter-propagating in the vertical symmetry plane, rays experience a variety of possible outcomes depending on the initial streamwise position relative to the dipole. Turning points are possible, but so is wave capture after the background horizontally reflects the propagation of a ray.

Co-propagating internal wave interactions with a vortex dipole jet resemble two-dimensional wave interactions with an accelerating shear flow [41]. This is especially so when rays approach the horizontal, as if at a critical level, despite increasing intrinsic frequency. Indeed, the components of group velocity behave like those of waves in an accelerating shear, with the vertical asymptotically approaching zero and the horizontal approaching the speed of the background. As this work shows, this indicates wave capture, which can be distinguished more fully by considering the exponential growth of the horizontal and vertical wavenumbers as waves interact with a vortex dipole. Work on wave capture has shown that this phenomenon occurs as the aspect ratio of the internal waves approaches the aspect ratio of the dipole, or $\left|\sqrt{k^2+l^2}/m\right| = L_v/H$ [27], but confirmation in this study has not been successful.

In another two-dimensional study on internal waves in an accelerating shear flow, the accelerated decrease of vertical wavenumber was shown to cause steepening of internal waves while simultaneously competing with damping waves because the background is absorbing the wave energy [33]. Ultimately, static instabilities are realized in the fluid, but absorption seems to occur before breaking can begin. In fact, about 90% of the decrease in wave energy results from

transfer to the background. This supports the possibility that waves are absorbed at a critical level when they enter the dipole jet from behind the translating dipole and first approach the horizontal. Though the vertical wavenumber of the "Dipole Rear" ray increases throughout the interaction, it may increase if absorption occurs as the wave packet approaches the critical level. As absorption is a nonlinear interaction, ray theory does not predict it.

Ray tracing also shows that, away from the vertical symmetry plane, internal wave energy is not limited to defocusing when internal waves co-propagate with a vortex dipole or to focusing when internal waves counter-propagate. The location of entrance into the vortex-dipole by off-center internal waves affects the subsequent spanwise refractions. For example, the co-propagating "Dipole Front" rays initiated at $y_0 \leq 0.11$ m refract multiple times in the spanwise direction (probable wave trapping [28]) and ultimately defocus, whereas rays initiated farther from the vertical symmetry plane primarily focus. Rays outside the vertical symmetry plane for the counter-propagating cases considered ($x_0 = -0.1$ m to $x_0 = 0.1$ m) also experienced focusing and/or defocusing depending on the initial spanwise position relative to the dipole. Outer rays initiated at about $y_0 \geq 0.1$ m, depending on the initial streamwise position, defocused while those closer to the vertical symmetry plane focused. Some rays seem to have also experienced multiple spanwise refractions that would be expected during wave trapping.

Focusing and defocusing were not simultaneously witnessed during the experiment, possibly because the experiment captured visual data only in the horizontal midplane while the ray tracing visualizes the entire depth of the domain. Moreover, the experimental view only showed a width spanning about $y = \pm 0.13$ m, slightly wider than the range of initial spanwise positions for which co-propagating rays defocus (at least when interacting with the front of the dipole) and counter-propagating rays focus. It is also reasonable that, because of the continuously propagating nature of the wave beam in the experiment, the top-down view of the co-propagating internal wave interaction would be dominated by wave energy entering the dipole later in the interaction. If so, observed wave energy may have entered the dipole from behind, corresponding to the "Dipole Rear" rays which principally defocus, agreeing with the experiment regardless of the initial spanwise position.

In co- and counter-propagating interactions, the wave steepness increases for several of the rays modeled, especially for most of those interacting along the vertical symmetry plane. However,

in considering wave steepness, wave capture, and the slow variation of wave properties, wave breaking or absorption may be possible, but not definite. Nevertheless, unless such nonlinearities arise, the traced spatial trajectories are trustworthy [26].

Despite its linear shortcomings, three-dimensional ray theory proves useful in understanding much of the mechanics involved in internal wave-vortex dipole interactions. By tracking the changes to properties of waves interacting with the dipole jet, ray theory agrees with experimental data on the possible existence of critical levels in the vertical symmetry plane during co-propagating interactions, but it also suggests the possibility of wave capture. It also confirms the possibility of turning points and introduces the possibility of wave capture in counter-propagating interactions. Additionally, three-dimensional ray tracing broadens understanding of the refractions of off-center rays in co- and counter-propagating interactions. It shows that these rays can experience multiple horizontal refractions similar to wave trapping, and focusing and defocusing depend on initial wave properties and initial positions relative to the vortex dipole rather than exclusively on the horizontal direction of internal wave propagation relative to the dipole.

The nature of internal wave-vortex interactions mandates that, for completeness and accuracy, experimental and numerical simulations be three-dimensional. Much more can and should be done to understand these and other three-dimensional internal wave interactions. While the experiment preceding this work was, of course, three-dimensional, the particle image velocimetry was limited to a few planes. One can then only estimate or infer the dynamics of the interactions outside of these planes. Newer methods, such as three-dimensional particle image velocimetry, should be pursued and developed such that results can be trusted. This would certainly increase the knowledge base of common physical interactions in the ocean and atmosphere which may otherwise be misunderstood. As another method, a three-dimensional nonlinear model would increase information regarding some of the stronger refractions experienced as a result of three-dimensional accelerations in the vortices. This would especially improve the understanding of wave amplitude changes during wave capture and wave turning. These methods may also help to more fully understand the assumptions needed in ray theory, including multi-dimensional factors for the slowly varying approximation (see Appendix A). Additional work may also strengthen confirmation of wave capture and wave trapping through matching the aspect ratios of the interacting phenomena [27, 28]. For interactions along the vertical symmetry plane, an analysis of hundreds

or even thousands of rays may yield a great understanding that could explain the circumstances under which one may expect the various phenomena possible during internal wave-vortex dipole interactions.

REFERENCES

[1] Garrett, C., and Munk, W., 1975. "Space-time scales of internal waves: A progress report." *Journal of Geophysical Research,* **80**, pp. 291–297. 1

[2] Dörnbrack, A., 1998. "Turbulent mixing by breaking gravity waves." *Journal of Fluid Mechanics,* **375**, pp. 113–141. 1

[3] Alford, M. H., 2003. "Redistribution of energy available for ocean mixing by long-range propagation of internal waves." *Nature,* **423**, pp. 159–162. 1

[4] Munk, W. H., and Wunsch, C., 1998. "Abyssal Recipes II: Energetics of tidal and wind mixing." *Deep-Sea Research,* **45**, pp. 1977–2010. 1

[5] Jeffreys, H., 1920. "Tidal friction in shallow seas." *Philosophical Transactions of the Royal Society of London. Series A,* **221**, pp. 239–264. 1

[6] Egbert, G. D., and Ray, R. D., 2000. "Significant dissipation of tidal energy in the deep ocean inferred from satellite altimeter data." *Nature,* **405**, pp. 775–778. 1

[7] Garrett, C., and Munk, W., 1979. "Internal waves in the ocean." *Annual Review of Fluid Mechanics,* **11**, pp. 339–369. 1

[8] Stewart, R. H., 2003. *Introduction to Physical Oceanography*. Texas A&M University. 1

[9] Gill, A. E., 1982. *Atmosphere-Ocean Dynamics*. Academic Press. 1, 4, 65

[10] Nappo, C. J., 2002. *An Introduction to Atmospheric Gravity Waves*., Vol. 85 Academic Press. 1, 6

[11] Sutherland, B. R., 2010. *Internal gravity waves*. Cambridge University Press. 1, 46, 53

[12] Bell, T. H., 1975. "Topographically generated internal waves in the open ocean." *Journal of Geophysical Research,* **80**, pp. 320–327. 6

[13] Maxworthy, T., 1980. "On the formation of nonlinear internal waves from the gravitational collapse of mixed regions in two and three dimensions." *Journal of Fluid Mechanics,* **375**, pp. 113–141. 6

[14] Kantha, L. H., 1979. "On generation of internal waves by turbulence in the mixed layer." *Dynamics of Atmospheres and Oceans,* **3**, pp. 39–46. 6

[15] Snyder, C., Muraki, D. J., Plougonven, R., and Zhang, F., 2007. "Inertia-gravity waves generated within a dipole vortex." *Journal of the Atmospheric Sciences,* **64**, pp. 4417–4431. 6

[16] Afanasyev, Y., 2003. "Spontaneous emission of gravity waves by interacting vortex dipoles in a stratified fluid: Laboratory experiments." *Geophysical and Astrophysical Fluid Dynamics,* **97**, pp. 79–95. 6

[17] Zhong, L., Sonmor, L. J., Manson, A. H., and Meek, C. E., 1995. "The influence of time-dependent wind on gravity-wave propagation in the middle atmosphere." *Annales Geophysicae,* **13**, pp. 375–394. 6

[18] Lombard, P. N., and Riley, J. J., 1996. "On the breakdown into turbulence of propagating internal waves." *Dynamics of Atmospheres and Oceans,* **23**, pp. 345–355. 6

[19] Staquet, C., and Sommeria, J., 2002. "Internal gravity waves: from instabilities to turbulence." *Annual Review of Fluid Mechanics,* **34**, pp. 559–593. 6, 9, 25, 38

[20] Garrett, C., 2003. "Mixing with latitude." *Nature,* **422**, pp. 477–478. 6

[21] Olbers, D. J., 1981. "The propagation of internal waves in a geostrophic current." *Journal of Physical Oceanography,* **11**, pp. 1224–1233. 6

[22] Thorpe, S. A., 1981. "An experimental study of critical layers." *Journal of Fluid Mechanics,* **103**, pp. 321–344. 6

[23] Javam, A., Imberger, J., and Armfield, S. W., 2000. "Numerical study of internal wave-wave interactions in a stratified fluid." *Journal of Fluid Mechanics,* **415**, pp. 65–87. 6

[24] Booker, J. R., and Bretherton, F. P., 1967. "The critical layer for internal gravity waves in a shear flow." *Journal of Fluid Mechanics,* **27**, pp. 513–539. 7

[25] Godoy-Diana, R., Chomaz, J. M., and Donnadieu, C., 2006. "Internal gravity waves in a dipolar wind: a wave-vortex interaction experiment in a stratified fluid." *Journal of Fluid Mechanics,* **548**, pp. 281–308. 7, 8, 15, 18, 26, 27, 28, 29, 31, 32, 39, 46, 47, 51, 52, 53, 54, 55, 65, 66

[26] Sartelet, K. N., 2003. "Wave propagation inside an inertia wave. Part I: Role of time dependence and scale separation." *Journal of the Atmospheric Sciences,* **60**, pp. 1433–1447. 9, 18, 59, 65

[27] Bühler, O., 2009. *Waves and Mean Flows*. Cambridge University Press. 9, 37, 57, 59

[28] Moulin, F. Y., and Flór, J. B., 2006. "Vortex-wave interaction in a rotating stratified fluid: Wkb simulations." *Journal of Fluid Mechanics,* **563**, pp. 199–222. 9, 14, 15, 42, 58, 59

[29] Broutman, D., 1986. "On internal wave caustics." *Journal of Physical Oceanography,* **16**, pp. 1625–1635. 11, 20

[30] Thorpe, S. A., 1999. "On the breaking of internal waves in the ocean." *Journal of Physical Oceanography,* **29**, pp. 2433–2441. 11

[31] Slinn, D. N., and Riley, J. J., 1996. "Turbulent mixing in the oceanic boundary layer caused by internal wave reflection from sloping terrain." *Dynamics of Atmospheres and Oceans,* **24**, pp. 51–62. 12

[32] Thorpe, S. A., 1978. "On internal gravity waves in an accelerating shear flow." *Journal of Fluid Mechanics,* **88**, pp. 623–639. 12

[33] Bouruet-Aubertot, P., and Thorpe, S. A., 1999. "Numerical experiments on internal gravity waves in an accelerating shear flow." *Dynamics of Atmospheres and Oceans,* **29**, pp. 41–63. 12, 57

[34] Bühler, O., and McIntyre, M., 2005. "Wave capture and wave-vortex duality." *Journal of Fluid Mechanics,* **534**, pp. 67–95. 12, 13, 37, 38, 39, 50

[35] Marks, C. J., and Eckermann, S. D., 1995. "A three-dimensional nonhydrostatic ray-tracing model for gravity waves: Formulation and preliminary results for the middle atmosphere." *Journal of the Atmospheric Sciences,* **52**, pp. 1959–1984. 14

[36] Winters, K. B., and D'Asaro, E. A., 1989. "Two-dimensional instability of finite amplitude internal gravity wave packets near a crtical level." *Journal of Geophysical Research,* **94**, pp. 709–712,719. 14

[37] Winters, K. B., and D'Asaro, E. A., 1994. "Three-dimensional wave instability near a critical level." *Journal of Fluid Mechanics,* **272**, pp. 255–284. 14

[38] Hayes, W. D., 1970. "Kinematic wave theory." *Proceedings of the Royal Society of London. Series A, Mathematical and Physical Sciences,* **320**, pp. 209–226. 17, 20

[39] Lighthill, J., 2003. *Waves in Fluids*. Cambridge University Press. 18, 20

[40] Pedlosky, J., 2003. *Waves in the Ocean and Atmosphere: Introduction to Wave Dynamics*. Springer-Verlag. 19

[41] Broutman, D., 1984. "The focusing of short internal waves by an inertial wave." *Geophysical and Astrophysical Fluid Dynamics,* **30**, pp. 199–225. 20, 57, 66

[42] Broutman, D., and Grimshaw, R., 1988. "The energetics of the interaction between short small-amplitude internal waves and inertial waves." *Journal of Fluid Mechanics,* **196**, pp. 93–106. 20

[43] Broutman, D., and Young, W. R., 1986. "On the interaction of small-scale oceanic internal waves with near-inertial waves." *Journal of Fluid Mechanics,* **166**, pp. 341–358. 20

[44] Whitham, G. B., 1965. "Nonlinear dispersive waves." *Proceedings of the Royal Society of London,* **283**, pp. 238–261. 20

[45] Meleshko, V. V., and Van Heijst, G. J. F., 2007. "On Chaplygin's investigations on coherent vortex structures." *Regular and Chaotic Dynamics,* **12**, pp. 226–232. 28

[46] Chaplygin, S. A., 1903. "One case of vortex motion in fluid." *Transactions of the Physical Section of Moscow Society of Friends of Natural Sciences, Anthropology and Ethnography,* **11**, pp. 11–14. 28

[47] Sartelet, K. N., 2003. "Wave propagation inside an inertia wave. Part II: Wave breaking." *Journal of the Atmospheric Sciences,* **60**, pp. 1448–1455. 38, 39

[48] Sutherland, B. R., and Yewchuk, K., 2004. "Internal wave tunneling." *Journal of Fluid Mechanics,* **511**, pp. 125–134. 54

[49] Broutman, D., Rottman, J. W., and Eckermann, S. D., 2004. "Ray methods for internal waves in the atmosphere and ocean." *Annual Review of Fluid Mechanics,* **36**, pp. 233–253. 66

APPENDIX A. VALIDITY OF RAY THEORY

Two assumptions must hold for ray theory to be valid. These are the scale separation hypothesis and the slowly varying approximation, an effect of the WKBJ approximation. The scale separation hypothesis requires that the temporal and spatial scales of internal waves be sufficiently different to those of the background in which they interact so that their features might remain distinct. Scaling factors have been suggested to test this hypothesis for internal wave interactions [26]. These are the streamwise horizontal scale factor $S_k = kR >> 1$, the spanwise horizontal scale factor $S_l = lR >> 1$, the vertical scale factor $S_m = mL_v >> 1$, and the temporal scale factor $S_f = \omega_r/f >> 1$ (the horizontal scale factors have been interpreted as such based on the vertical scale factor). However, since the rotational frequency f of the fluid is zero in this work, the temporal scaling is ignored.

Initially, spatial scaling violates the scale separation hypothesis. However, as rays experience turning points or wave capture in the vertical symmetry plane the scale factors sharply approach infinity. For a co-propagating ray approaching a critical level in the vertical symmetry plane, the vertical scale factor also quickly increases to infinity, but the streamwise horizontal scale factor decreases unless the ray escapes the critical level and approaches wave capture, at which time the streamwise scale factor approaches infinity. Wave trapping of co- and counter-propagating rays outside the vertical symmetry plane does not significantly affect the scale factors any more than other horizontal refractions. In any case, as long as internal waves do not experience nonlinearities, such as energy absorption by the dipole or wave breaking, the ray trajectories remain correct [26]. Also, the scale separation hypothesis is assumed valid because Godoy-Diana, et al. [25] found only negligible changes to the vortex dipole during any interaction.

The slowly varying approximation requires that changes in amplitude from one wave to the next have little variation within a wave packet [9]. It assumes that wave steepness remains finite throughout the wave evolution. Typically, it follows the assumption that the fractional changes

in a given wave property are small relative to the reciprocal of that wave property [41]; that is, $\left|\omega_r^{-2}\partial\omega_r/\partial t\right| << 1$, $\left|k^{-2}\partial k/\partial x\right| << 1$, $\left|l^{-2}\partial l/\partial y\right| << 1$ and $\left|m^{-2}\partial m/\partial z\right| << 1$. However, it is uncertain what the proper forms of the fractional changes are in multiple dimensions [49].

In general, rays in this work are within these bounds, though exceptions arise when some rays, co- and counter-propagating, initiated within 10 or 15 centimeters of the vertical symmetry plane, including $y_0 = 0$ cm, experience a sudden increase in one or more of these factors. These occur during moments of stronger refraction, such as when approaching a critical level, wave capture, wave trapping, or a turning point. This is not surprising, however, since the infinite wave steepness predicted by ray theory breaks down the slowly varying approximation [49]. Though the slowly varying approximation is necessary for accurate calculations in ray theory, the results of this study generally agree with the experiment [25] and the assumptions regarding these fractional changes may not always be appropriate for internal wave-vortex dipole interactions.

APPENDIX B. DERIVATION OF WAVE SOLUTION

Assumptions

Incompressible fluid, inviscid fluid ($Re >> 1$), Boussinesq approximation (i.e., keep ρ' only when multiplied by g)

Density

$$\rho = \rho_0 + \bar{\rho}(z) + \rho'(x,y,z,t) \tag{B.1}$$

where $\bar{\rho}(z) = \rho_1 - \rho_0$ is the density distribution, $\rho'(x,y,z,t) = \rho_1 - \rho_2$ is the perturbation density, ρ_0 is a reference density, ρ_1 is the density of the displaced fluid particle, and ρ_2 is the density of the fluid surrounding the displaced particle after it is perturbed (see Figure B.1). Note $\bar{\rho} << \rho_0$ and $\rho' << \rho_0$ such that

$$\frac{\rho}{\rho_0} = 1 + \frac{\bar{\rho}}{\rho_0} + \frac{\rho'}{\rho_0} \approx 1 \tag{B.2}$$

Pressure (gauge)

$$p = \bar{p} + p' \tag{B.3}$$

where $\bar{p}$ is in hydrostatic balance (i.e., $\partial \bar{p}/\partial z = -(\rho_0 + \bar{\rho})g$) and p' is the perturbation pressure.

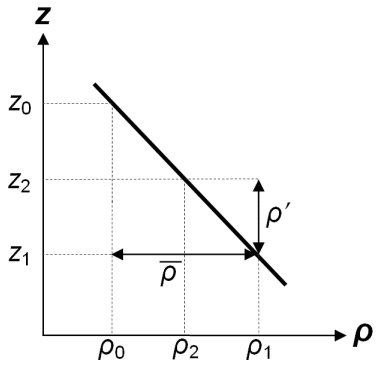

Figure B.1: Schematic of density distribution.

Conservation of Momentum and Mass

$$\rho\frac{Du}{Dt} = -\frac{\partial p}{\partial x}+\mu\left(\frac{\partial^2 u}{\partial x^2}+\frac{\partial^2 u}{\partial y^2}+\frac{\partial^2 u}{\partial z^2}\right)=-\frac{\partial p}{\partial x} \tag{B.4}$$

$$\rho\frac{Dv}{Dt} = -\frac{\partial p}{\partial y} \tag{B.5}$$

$$\rho\frac{Dw}{Dt} = -\frac{\partial p}{\partial z}-\rho g \tag{B.6}$$

$$\nabla\cdot\boldsymbol{u} = 0 \tag{B.7}$$

$$\frac{D\rho}{Dt} = \frac{\partial\rho}{\partial t}+(\boldsymbol{u}\cdot\nabla)\rho = 0 \tag{B.8}$$

where $\boldsymbol{u}=(u,v,w)$ is the velocity vector of the internal wave packet and μ is the dynamic viscosity of the fluid.

Boussinesq Navier-Stokes Equations

Sub Equations B.1 and B.3 into the conservation of momentum and conservation of mass equations. Apply the Boussinesq approximation and rearrange.

$$\frac{Du}{Dt} = -\frac{1}{\rho_0}\frac{\partial p'}{\partial x} \tag{B.9}$$

$$\frac{Dv}{Dt} = -\frac{1}{\rho_0}\frac{\partial p'}{\partial y} \tag{B.10}$$

$$\frac{Dw}{Dt} = -\frac{1}{\rho_0}\frac{\partial p'}{\partial z} - \frac{\rho'}{\rho_0}g \tag{B.11}$$

$$\frac{\partial u}{\partial x} + \frac{\partial v}{\partial y} + \frac{\partial w}{\partial z} = 0 \tag{B.12}$$

$$\frac{\partial \rho'}{\partial t} + w\frac{\partial \bar{\rho}}{\partial z} = 0 \tag{B.13}$$

Linear Boussinesq Navier-Stokes Equations

To linearize, assume small amplitude, i.e., $u, v, w = O(\varepsilon)$, and small convective acceleration, i.e., $\boldsymbol{u} \cdot \nabla \boldsymbol{u} = O\left(\varepsilon^2\right)$ such that

$$\begin{aligned}
\frac{Du}{Dt} &= \frac{\partial u}{\partial t} + \boldsymbol{u} \cdot \nabla u \approx \frac{\partial u}{\partial t} \\
\frac{Dv}{Dt} &= \frac{\partial v}{\partial t} + \boldsymbol{u} \cdot \nabla v \approx \frac{\partial v}{\partial t} \\
\frac{Dw}{Dt} &= \frac{\partial w}{\partial t} + \boldsymbol{u} \cdot \nabla w \approx \frac{\partial w}{\partial t}
\end{aligned}$$

Sub into Equations B.9 through B.11:

$$\frac{\partial u}{\partial t} = -\frac{1}{\rho_0}\frac{\partial p'}{\partial x} \tag{B.14}$$

$$\frac{\partial v}{\partial t} = -\frac{1}{\rho_0}\frac{\partial p'}{\partial y} \tag{B.15}$$

$$\frac{\partial w}{\partial t} = -\frac{1}{\rho_0}\frac{\partial p'}{\partial z} - \frac{\rho'}{\rho_0}g \tag{B.16}$$

$$\frac{\partial u}{\partial x} + \frac{\partial v}{\partial y} + \frac{\partial w}{\partial z} = 0 \tag{B.17}$$

$$\frac{\partial \rho'}{\partial t} + w\frac{\partial \bar{\rho}}{\partial z} = 0 \tag{B.18}$$

Wave Equation

Take the time derivative of Equation B.16:

$$\frac{\partial^2 w}{\partial t^2} = -\frac{1}{\rho_0}\frac{\partial^2 p'}{\partial t \partial z} - \frac{g}{\rho_0}\frac{\partial \rho'}{\partial t} \tag{B.19}$$

Sub from the Equation B.18 and rearrange for

$$\frac{\partial^2 w}{\partial t^2} + N^2 w = -\frac{1}{\rho_0}\frac{\partial^2 p'}{\partial t \partial z} \tag{B.20}$$

where N is the buoyancy frequency of the fluid (see Equation 1.2 and the accompanying discussion).

Sum the spatial derivatives of Equations B.14 and B.15:

$$\frac{\partial}{\partial t}\left(\frac{\partial u}{\partial x} + \frac{\partial v}{\partial y}\right) = -\frac{1}{\rho_0}\left(\frac{\partial^2}{\partial x^2} + \frac{\partial^2}{\partial y^2}\right) p' \tag{B.21}$$

Sub from Equation B.12 and let $\nabla_H^2 = \partial^2/\partial x^2 + \partial^2/\partial y^2$ be the horizontal gradient operator:

$$\frac{\partial^2 w}{\partial t \partial z} = \frac{1}{\rho_0}\nabla_H^2 p' \tag{B.22}$$

Apply the horizontal gradient operator to Equation B.20, sub from Equation B.22, and rearrange to yield the wave equation

$$\frac{\partial^2 \left(\nabla^2 w\right)}{\partial t^2} + N^2 \nabla_H^2 w = 0 \tag{B.23}$$

The solution to the wave equation, symmetric in the horizontal and assymetric in the vertical, is given by

$$w = w_0 \cos(\vec{k} \cdot \vec{x} - \omega t) \tag{B.24}$$

where w is the verical component of the background velocity and the subscript 0 represents the inital value, $\boldsymbol{k}$ is the wavenumber vector, $\boldsymbol{x}$ is the spatial vector, ω_r is the relative frequency of the small-scale internal waves, and t is time.